Wadas and von Hartmann
Geothermal Energy (2022) 10:13
https://doi.org/10.1186/s40517-022-00223-5

Geothermal Energy

RESEARCH Open Access

Porosity estimation of a geothermal carbonate reservoir in the German Molasse Basin based on seismic amplitude inversion

Sonja Halina Wadas* and Hartwig von Hartmann

*Correspondence:
sonja.wadas@leibniz-liag.de

Leibniz Institute for Applied Geophysics, Stilleweg 2, 30655 Hannover, Germany

Abstract

The Molasse Basin is one of the most promising areas for deep geothermal exploitation in Germany and the target horizon is the aquifer in the Upper Jurassic carbonates. Carbonate deposits can be very heterogeneous even over a small area due to diagenetic processes and varying depositional environments. The preferential targets for geothermal exploitation in carbonate deposits are fault zones, reef facies and karstified areas, since they are expected to act as hydraulically permeable zones due to high porosity and high permeability. Therefore, identifying these structures and characterizing, e.g., their internal porosity distribution are of high importance. This can be accomplished using 3D reflection seismic data. Besides structural information, 3D seismic surveys provide important reservoir properties, such as acoustic impedance, from which a porosity model can be derived. In our study area in Munich we carried out a seismic amplitude inversion to get an acoustic impedance model of the Upper Jurassic carbonate reservoir using a 3D seismic data set, a corresponding structural geological model, and logging data from six wells at the 'Schäftlarnstraße' geothermal site. The impedance model and porosity logs were than used to calculate a porosity model. The model shows a wide porosity range from 0 to 20% for the entire reservoir zone and the lithology along the wells reveals that dolomitic limestone has the highest porosities and calcareous dolomite has the lowest porosities. The study area is cut by a large W–E striking fault, the Munich Fault, and the footwall north of it shows higher porosities and more intense karstification than the hanging wall to the south. Considering the entire study area, an increase in porosity from east to west is observed. Furthermore, we identified a complex porosity distribution in reef buildups and pinnacle reefs. The reef cores have mostly low porosities of, e.g., < 3% and the highest porosities of up to 7 to 14% are observed at the reef caps and on the reef slopes. The reef slopes show a characteristic interfingering of the reef facies with the surrounding bedded facies, which indicates a syn-sedimentary reef development with slightly varying build up growth rates. We also assessed the reservoir quality with regard to porosity distribution and determined areas with moderate to good quality for geothermal exploitation by defining porosity evaluation levels. The porosity evaluation maps show that the carbonate rocks of Berriasian to Malm ζ1 are preferential targets for exploitation, especially in the footwall of the Munich Fault and to the west of the hanging wall, because these

areas are characterized by high porosities due to intense karstification of bedded and massive facies, although the latter is mainly restricted to reef caps and reef slopes.

Keywords: German Molasse Basin, Geothermal reservoir, Jurassic carbonates, Seismic amplitude inversion, Porosity, Reef buildup, Karstification, Munich

Introduction

Geothermal energy can play an important role by providing climate-friendly energy and heat supplies from renewable sources. In Germany high temperatures and good hydraulic conditions occur in the North German Basin, the Upper Rhine Graben, and the South German Molasse Basin (Agemar et al. 2012). The main acquifer for hydrothermal exploitation in the German Molasse Basin (GMB) is located within the Upper Jurassic Malm carbonates (Stober and Villinger 1997; Jodocy and Stober 2009; Stober et al. 2013; Steiner et al. 2014; Stober 2014). The preferential targets in carbonate deposits of the GMB are fault zones, reef facies and karstified areas, since they are expected to act as hydraulically permeable zones due to high porosity and high permeability (Lüschen et al. 2011; Birner et al. 2012; Böhm et al. 2013; Homuth et al. 2015; Moeck et al. 2020). One of the most ambitious projects in the GMB is the creation of a CO_2 emission-free district heating network for the city of Munich by 2040. To reach this goal the use of geothermal energy must be further expanded (Kenkmann et al. 2017; Dufter et al. 2018).

However, it can be difficult to predict porosity and permeability which describe the geothermal potential, because of the heterogeneous nature of the carbonate deposits and the effects of diagenetic processes. In general, carbonates can have a wide range of porosities from almost 0% in tightly cemented rocks to about 35% in unconsolidated sediments (Lucia 2007). Porosity can be either primary or secondary porosity (Lucia 2007). Primary porosity is the pore space between grains that was generated during the time of deposition (e.g., interparticle-, intraparticle-, growth framework-, shelter- and fenestral porosity), and secondary porosity is the pore space that was formed after deposition of the sediments due to, e.g., geological and/or diagenetic processes (e.g., moldic-, channel-, intercrystalline-, fracture- and vuggy porosity) (Lucia 2007). The diagenetic processes affecting porosity are cementation, compaction, dolomitization, and dissolution (Ghafoori et al. 2009). Cementation and compaction are main reason for porosity reduction in carbonates (Schmoker and Halley 1982; Wolfgramm et al. 2011; Homuth 2014) and dolomitization and dissolution can have the opposite effect (Lucia et al. 1992; Koltermann and Gorelick 1996; Eaton 2006; Mraz 2019). During dolomitization calcite is replaced by dolomite leading to a reduction of the rock volume and, therefore, an increase of the total porosity by creating secondary porosity (Sajed and Glover 2020), and the percolation of unsaturated water can lead to the dissolution of calcite or aragonite, and the formation of secondary porosity and even large cavities (Kendall and Schlager 1981; Xu et al. 2017). Besides diagenetic processes, the variability of porosity, and also permeability, is also influenced by spatial variation of karstification intensity and the distribution of facies types (e.g., reef facies is often more prone to karstification; Birner et al. (2012); Böhm et al. (2013); Homuth et al. (2015)). As a result, in most cases no general trends describing the porosity–permeability relationship in carbonates based on stratigraphic units or lithology can be determined. This circumstance has already been described by Ehrenberg and

Nadeau (2005); Homuth (2014); Bohnsack et al. (2020) and Moeck et al. (2020) for the carbonate reservoir in the Upper Jurassic formations of the GMB, which is a mainly fracture- and karst-controlled reservoir. As a consequence, a simplified classification of a carbonate reservoir based on small samples, e.g., from cores (Homuth 2014), is often not sufficient, because they are unable to depict the entire range of reservoir heterogeneity. Instead, a sophisticated investigation approach is needed to depict the vertical and lateral differences in reservoir properties even in case of small-scale variations. As shown by numerous oil and gas exploration studies, 3D reflection seismic surveys can not only deliver structural information, but also important reservoir properties, e.g., elastic parameters and a variety of seismic attributes (Pussak et al. 2014; Marfurt 2015; Wang et al. 2015).

One of the most important seismic attributes is the acoustic impedance, from which a porosity model can be derived (Gogoi and Chatterjee 2019). Acoustic impedance can be calculated by seismic amplitude inversion, because the amplitudes of the reflected waves change, depending on the impedance contrast at an interface. Therefore, the reflection amplitudes can be used to invert the data to obtain impedance values. To accomplish this the seismic inversion uses seismic data as a constraint to extrapolate the impedance derived from logs and interpolate between them (Doyen 2007; Barclay et al. 2008). By correlating the derived impedance property with other borehole measurements other reservoir properties, such as the porosity, can be determined. Such a 3D porosity model can help to better understand the heterogeneous distribution of at least one of the two parameters (porosity and permeability) that influence the productivity of the reservoir, because so far no seismic method exists that is able to derive permeability values from seismic amplitudes or seismic inversion (Pride et al. 2003).

Seismic amplitude inversion, and the accompanied advanced structure- and rock property interpretation, is a common tool in oil and gas exploration that enables the prediction of, e.g., lithology, fluid content, and porosity, which can then be used to identify hydrocarbon targets and reservoirs (Dohlberg et al. 2000; Barclay et al. 2008; Mahgoub et al. 2017, 2018; Shankar et al. 2021). Nevertheless, seismic inversion is rarely applied in geothermal exploration worldwide, although this method has been known since the 70s, where it started with the classic post-stack inversion (Lindseth 1979). Examples for the successful application of seismic inversion for geothermal exploration were conducted, e.g., in Denmark (Bredesen et al. 2020) and Australia (Pavlova and Reid 2010), where 2D AVO inversion and 3D genetic inversion were used to improve reservoir characterization and to predict the porosity of sandstone formations. Despite its potentially great benefit, seismic inversion has not been used so far in geothermal exploration projects in Germany. However, to reduce the risk of failed projects in heterogeneous areas, it is necessary to characterise the subsurface in as much detail as possible, which can't be achieved using well data alone. Seismic inversion techniques provide a unique framework were the advantages of reflection seismic data and log data can be combined by delivering an impedance volume with a seismic-like areal resolution and a log-like vertical resolution (Robinson 2001).

In this paper, we illustrate the first application of seismic amplitude inversion to characterize a geothermal reservoir in Germany. We show for the case study of Munich and the 'Schäftlarnstraße' geothermal site in the GMB, that a 3D seismic survey in

combination with a seismic inversion is a powerful tool to predict porosity and to identify preferential targets for geothermal exploitation.

Geological setting

Regional geology

The region around Munich is located within the GMB (Fig. 1) in the North Alpine Foreland Basin, which extends over a distance of 1000 km from west to east and has a maximum width of about 150 km (Lemcke 1973). The area has experienced a complex sedimentary and structural evolution. It began with an initial Permo-Carboniferous graben phase that was followed by a Triassic to Middle Jurassic epicontinental or shelf phase, and a Middle Jurassic to Cretaceous passive margin phase. Finally, during the

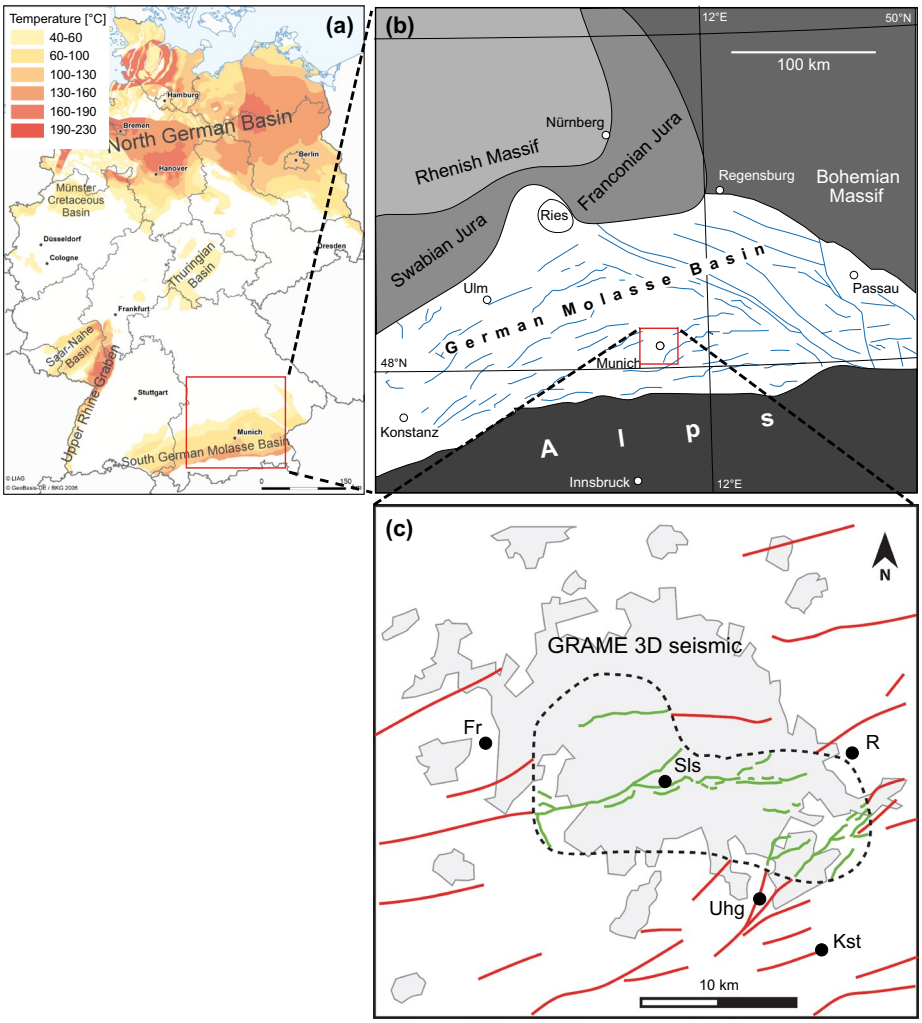

Fig. 1 The study area is located in the South German Molasse Basin (**a**; after Agemar et al., 2012) in the city of Munich (**b**, **c**). In 2016 a 170 km^2 3D seismic survey was conducted in Munich (outlined area with dashed line) to investigate and better understand the reservoir geometries and rock parameters. The colored lines are faults that result from strong tectonic deformation due to the Alpine orogeny (red: old known faults, green: newly identified faults from 3D seismic data interpreted by Ziesch (2019)). These might influence the reservoir and, therefore, geothermal production plants (Fr: Freiham, Kst: Kirchstockach, R: Riem, Sls: Schäftlarnstraße, Uhg: Unterhaching)

Tertiary foreland phase the Molasse Basin was formed (Bachmann et al. 1987; Bachmann and Müller 1992).

The basement is represented by gneiss formed during the Variscian Orogeny and post-orogenic granite intrusions (Lemcke 1988). This basement was segmented by SW–NE striking grabens during the Permian and the Carboniferous (Arthaud and Matte 1977; Ziegler 1990). During the Mesozoic, the area was part of an epicontinental ocean at the northwestern margin of the Thetys (Bachmann et al. 1987; Ziegler 1990; Freudenberger and Schwerd 1996). The Tethys, also called Neotethys, was an ocean which formed during the Late Triassic between the continents of Gondwana and Laurasia until it was closed in the Early Eocene (Hopley 2011). In Late Jurassic, the study area was completely inundated by the epicontinental ocean which was then connected to the Tethys Sea, forming a passive margin (Bachmann et al. 1987). During this time, up to 600 m of carbonates, also called Malm carbonates after the German term for the Upper Jurassic, were deposited, forming a carbonate platform in the study area (Schmid et al. 2005; Pieńkowski et al. 2008). The Malm can be subdivided into six cycles labelled alpha (α), beta (β), gamma (γ), delta (δ), epsilon (ϵ) and zeta (ζ), from bottom to top based on litho- and biostratigraphic criteria after Quenstedt (1858). Malm ζ can be further subdivided into $\zeta 1$ to $\zeta 6$. Thereby, Malm α and Malm β correspond to the stratigraphic unit of the Oxfordian, Malm γ to Malm ϵ correspond to the Kimmeridgian, and Malm ζ corresponds to the Tithonian. After a regression of the Tethys Ocean at the Jurassic–Cretaceous boundary (Bachmann et al. 1987; Bachmann and Müller 1992), marine sediments were deposited again in the Early Cretaceous forming the Purbeck of the Priabonian (Freudenberger and Schwerd 1996). From Late Cretaceous to Early Tertiary time southern Germany was uplifted, resulting in extensive compressional deformation due to the Alpine orogeny (Ziegler 1987).

The underthrusting of the European plate below the Adriatic–African plate in the Late Eocene caused the lateral extent of the Alpine nappes to the north, which led to subsidence-induced development of the Molasse Basin due to the load of the nappes (Frisch 1979). The development of the Molasse Basin was accompanied by two major transgressive–regressive cycles (Eisbacher 1974). Sediments deposited under marine conditions are called 'Marine Molasse' and are separated into the Lower Marine Molasse (UMM) and the Upper Marine Molasse (OMM). Sediments deposited in rivers and lakes are referred as 'Freshwater Molasse' and are separated into the Lower Freshwater Molasse (USM) and the Upper Freshwater Molasse (OSM). The UMM is Rupelian in age and consists of shallow marine sands, clays, and marls. It is overlain by the USM of Chattian and Aquitanian age consisting of mainly fluvial sands and clays, conglomerates and breccias. In the Early Miocene, during the second transgressive–regressive cycle, marine sand clays and marls of the OMM were deposited, overlain by the continental facies of the OSM in the Late Miocene consisting of fluvial sands and clays, and conglomerates (Lemcke 1988). Finally, the Molasse sediments were overlain by Pleistocene glacial and interglacial deposits. The Alpine tectonism produced a structural subdivision of the GMB into the Foreland Molasse, the Inclined Molasse and the Folded Molasse (Bachmann and Müller 1992). As a result of the compressional stress regime, antithetic and synthetic normal faults developed parallel to the Alpine front.

Site description

A detailed structural analysis of the 3D seismic data set GRAME by Ziesch (2019), shows that the Munich area is traversed by numerous structures most of which are normal faults (Fig. 1c). The Munich Fault, an extension of the Markt–Schwaben Lineament, is the largest fault in the study area with a maximum offset of 350 m. The Munich Fault splits into several branches subdividing the area around the 'Schäftlarnstraße' geothermal site (SLS) into a footwall block, an intermediate block and a hanging wall block. The fault system in the southeast of the study area, the Ottobrunn Fault, also splits into several small antithetic and synthetic faults with small offsets up to 80 m forming a horsetail splay. This indicates a combined normal fault- and strike-slip regime (Ziesch 2019). The dip angles of the faults change during the transition from the molasse sediments to the carbonates. While the faults in the molasse have dip angles of 55°to 65°, the faults in the carbonate reservoir are much steeper, with dips up to 80°. Thickness maps show a uniform thickness distribution for the Malm carbonates across the entire study area, while the molasse sediments on the hanging wall of the Munich Fault vary in thickness of up to 100 m compared to the footwall deposits. This indicates syn-sedimentary fault movement during the Tertiary (Ziesch 2019). Such complex fault patterns are also found at other geothermal sites in the GMB, e.g., at Unterhaching and Geretsried (Lüschen et al. 2011, 2014; Shipilin et al. 2020). At the 'Unterhaching' geothermal site an en-echelon pattern of left-stepping synthetic and antithetic normal faults, related to extensional stress induced by flexural bending of the crust during the Alpine orogeny, is observed (Lüschen et al. 2011, 2014). In addition, at the 'Geretsried' geothermal site two fault arrays are identified of which the lower one is situated in the Upper Jurassic carbonate deposits, and it consists of mainly steep-dipping normal faults and a graben structure defined by conjugate faults (Shipilin et al. 2020). This indicates that the Upper Jurassic carbonate deposits in the GMB are generally characterized by complex faulting.

The structural analysis of the 3D seismic data set GRAME also reveals the influence of karstification processes on the study area (Ziesch 2019). Karstification describes the dissolution of soluble rocks in the subsurface and the resulting formation of cavities that can lead to the generation of sinkholes in case of a cavity collapse. This process is often more intense close to faults, since the fracture zones surrounding them, in case of open fractures, can enhance fluid migration and, therefore, dissolution (Closson and Abou Karaki 2009; Del Prete et al. 2010; Wadas et al. 2017). In our study area, several isolated sinkholes located at fault terminations on top or within the carbonate deposits are imaged and also smaller sinkhole clusters, which are found further from the faults (Ziesch 2019). Similar observations on karstification processes of the carbonate deposits are made for the 'Unterhaching' geothermal site, where a 3D seismic survey revealed several sinkholes at the top of the Malm and especially along fault zones (Lüschen et al. 2011, 2014). In addition, outcrop studies, e.g., at the Franconian Alb, further prove that the Jurassic carbonates were affected by widespread karstification processes that influence the rock- and reservoir parameters, such as permeability and porosity (Homuth 2014; Mraz 2019).

Geothermal reservoir

The geothermal reservoir comprises of the 400 to 650 m thick Upper Jurassic formation (referred to as Malm—after the German term for the Upper Jurassic), which dips to the south. The depth of the carbonate reservoir in the greater Munich area varies between 1500 to 4500 m, resulting in a water temperature increase towards the south. As a consequence geothermal energy is used for heat generation in the Munich area and north of it, and south of Munich it can also be utilized for electricity generation. In general, the production temperatures range between approximately 70°C to 150°C (Böhm 2012; Homuth et al. 2015).

The Malm formation consists of calcareous and marly, partly dolomitized, carbonates that can be separated into two hyper facies types: a massive carbonate- (often consisting of large reefs) and a bedded carbonate facies (Reinhold 1998). Many studies have shown that the massive facies is a suitable target for geothermal exploitation, because the reefs are more prone to dolomitization and karstification. During the dolomitization process the recrystallisation leads to an increase in permeability and porosity, because the volume of dolomite is less than that of calcite. In addition, the karstification has also a direct influence on the reservoir parameters by enlarging pore space and fluid pathways due to dissolution of the carbonates. As a result, the reefs often exhibit improved porosity and permeability conditions with groundwater movement occurring mainly along karst cavities, joints, fractures, and fault zones, and to a lesser extent along bedding planes (Andres 1985; Birner et al. 2012). In addition, due to its petrophysical properties, the reef facies is more prone to brittle deformation, which facilitates the generation and propagation of fractures, e.g., due to the influence of the tectonic stress field. In general, the Upper Jurassic carbonates can be described as a lithology and facies dependent fracture- and karst-controlled reservoir.

A hydrostratigraphic classification of the Malm in the greater Munich area carried out by Böhm (2012) and based on a lithofacies differentiation shows that the lowermost units Malm α to Malm γ, which consist of partly marly limestones, can be characterized as an aquitard. Malm δ to Malm ϵ are described as a regional aquifer due to a laterally persistent dolomitic massive facies. In addition, Malm ζ contains local aquifers in dolomitized massive facies as well as aquitards in bedded limestones.

Information on net thickness, porosity or permeability in a karstified/fractured aquifer are very difficult to obtain, because they can vary significantly even over short distances. For that reason, mostly only regional and no local trends are described for the aforementioned parameters (Birner et al. 2012). For example, in the central GMB, average void volumes of 2.5% for the Malm can be expected (Hänel et al. 1984); a more recent study of core samples and well logs shows a high variance of effective porosity from 0.3 to 19.2% (Bohnsack et al. 2020).

Methodology

Seismic amplitude inversion

Seismic inversion, whose development began in the ’70s (Lindseth 1979), has been studied for decades as it is one of the most effective methods for reservoir characterization in seismic exploration (Pendrel 2001). The principle aim of seismic inversion is to transform seismic reflection data into a quantitative rock property, such as acoustic

impedance (Barclay et al. 2008). The inversion of seismic data offers several advantages compared to classical interpretation of reflection amplitudes, e.g., (1) the reduction of the effects of the wavelet tuning resulting in a subsurface model with higher resolution, (2) calibration to well log data and implementation of geophysical constraints, (3) an increased bandwidth of the inversion output due to implementation of frequencies beyond the seismic bandwidth, e.g., from well logs, (4) modelling and inclusion of layer stratigraphy and improved interpretability of horizons and geological structures, and (5) derived reservoir parameters based on a strong relationship between acoustic impedance and petrophysical properties (Pendrel and Van Riel 1997; Hill 2005).

Seismic inversion techniques can be classified by the type of the seismic data set (full stack- or partial stack seismic data) and by the mathematical approach (deterministic or stochastic approach). Inversion of full-stack seismic data enables the estimation of one elastic property (acoustic impedance) and with partial stack seismic data, which utilizes, e.g., amplitude variation with offset, multiple elastic properties, such as P-Impedance, S-Impedance, density and V_P/V_S ratio can be determined (Pendrel 2001; Filippova et al. 2011). Regarding the mathematical approach, the deterministic algorithms can only deliver results within the seismic bandwidth, while stochastic algorithms give results with an improved vertical resolution due to the implementation of frequencies beyond the seismic bandwidth (Pendrel 2001; Jarvis et al. 2004; Francis 2006a, b; Filippova et al. 2011). Furthermore, the deterministic approach delivers only a least-squares solution, while the stochastic approach uses a broad-band starting model, with, e.g., well-log based a-priori information, and it applies a global-search method that calculates multiple realizations, each trying to minimize the mismatch between the synthetic data and the seismic data to find the best-fitting result (Francis 2006a, b; Doyen 2007; Barclay et al. 2008; Zhang et al. 2012). A more detailed overview of different inversion techniques is given by, e.g., Pendrel (2001); Barclay et al. (2008); Filippova et al. (2011).

In this study, the aim was to characterize the carbonate reservoir in as much detail as possible; therefore, a full-stack stochastic inversion was applied (no partial stack seismic data was available). In detail, the stochastic seismic amplitude inversion, which was originally developed by Haas and Dubrule (1994), uses seismic data as a constraint to extrapolate the impedance derived from logs and interpolate between them. A comprehensive explanation is given by Barclay et al. (2008) and Doyen (2007). The stratigraphic grid for the discretization of the inversion process has a higher vertical resolution than the band-limited seismic data can provide. This obstacle is overcome by implementing frequency data beyond the seismic bandwidth to get broad-band inversion results with high vertical resolution of, e.g., 2 ms (Rashad et al. 2022). Two typical input data sets for reconstruction of the missing frequency data are well log data and seismic velocity data. Well log data such as sonic and density logs contain a full range of frequencies from zero to greater than the seismic bandwidth (Sams and Carter 2017). The well data is interpolated into the stratigraphic grid and serves as a starting model for the global-search method of the inversion process. The process of interpolation and extrapolation, and therefore, the distribution of the physical parameters, is based on kriging and on a sequential Gaussian simulation (Haas and Dubrule 1994). Along random paths in the survey area, sequences of seismic reflections are calculated, convolved with a seismic wavelet, and compared with the actual seismic trace. The intermediate result is the

actual best fit with the seismic trace. Traces at the wells and close to the wells are constraints of the next random paths. The simulation of traces is repeated until an inversion result was calculated for each seismic trace of the entire data set. This procedure is carried out repeatedly and the best correlations at every trace location of all realizations deliver the final impedance model.

It should be noted that seismic inversion is a non-unique process; therefore, there is no single solution for the inverse problem (Veeken and Da Silva 2004). Different acoustic impedance models can be consistent with the input data (e.g., seismic data, logging data, and wavelet). This non-uniqueness problem can be partially solved by implementing constraints, e.g., from wells (Nascimento et al. 2014), that reduce the number of possible solutions to get the best-fitting result. In stochastic inversion these non-unique solutions are called realizations, whose mean or average delivers the final result that comes closest to reality (Veeken and Da Silva 2004).

Database

This study is based on a 170 km^2 3D seismic survey measured across Munich and borehole data from six wells from the 'Schäftlarnstraße' geothermal site (SLS). The seismic data was acquired and processed by DMT Petrologic GmbH (Scholze and Wolf 2016a, b). For the 3D data acquisition (Table 1) a dense source and receiver spacing with line distances of 400 to 500 m, a source spacing of 50 m and a receiver group spacing of around 50 m were used, and a comprehensive data processing was utilized, resulting in a 3D seismic cube with high-resolution of around 40 m to 50 m in the reservoir formation and a good signal-to-noise ratio. Important processing steps (Table 2) consisted of a migration velocity analysis using a tomographic inversion (Yilmaz 2001) which delivered the final velocity model for the following Kirchhoff Pre-Stack Depth-Migration (PreSDM; Yilmaz (2001)). To obtain the final velocity model, the velocity model from the Pre-Stack Time-Migration was used as the initial velocity model and was then smoothed at four horizons between 300 m and 2000 m depth. With the tomographic inversion, the velocity model was then recalculated based on the residual-moveout from image gathers and a ray tracing that took the refraction of the seismic rays into account (Hill and Rüger 2019).

The six wells of the geothermal plant at the site SLS, which is currently under construction, were geologically investigated and geophysically surveyed. The available data includes, e.g., stratigraphic and lithological information and sonic logs (Böhm and Dax 2019; SWM 2019; Schölderle et al. 2021).

The PreSDM cube in combination with the sonic logs (both converted into time domain) were used to carry out the stochastic seismic amplitude inversion to get an acoustic impedance volume. Later on, the logging data was also utilized to define the relationship between acoustic impedance and porosity, to get a function that could be used to calculate a 3D porosity model.

Workflow

An overview of the complex inversion workflow is shown in Fig. 2 and will be explained in more detail in the following section.

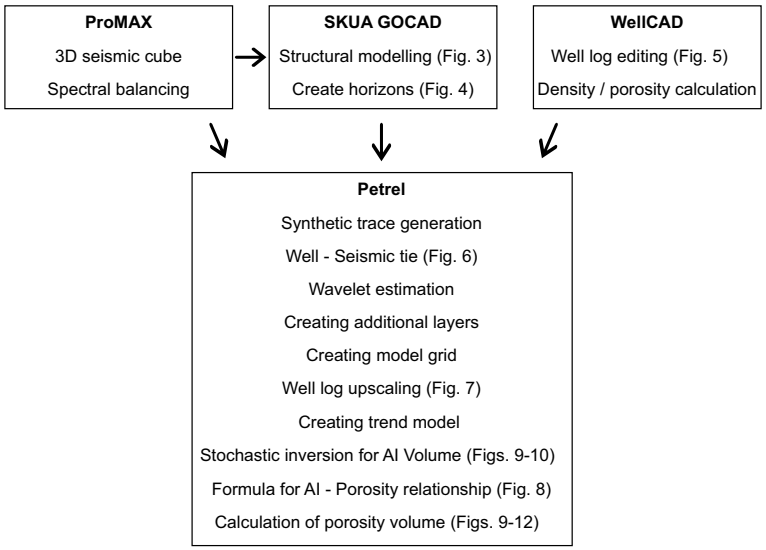

Fig. 2 Workflow utilized to perform the full-stack stochastic seismic amplitude inversion with references to the corresponding illustrations

Table 1 Acquisition parameters of the GRAME 3D seismic

Acquisition parameters	
Survey area	171.906 km^2
Seismic source	3x AHV-IV PLS362 vibrators
Source spacing	50 m
Source line distance	400–500 m
Sweep	12–95 Hz, linear
Sweeps per source point	9 for each of the 3 vibrators
Receiver type	Geophon Sercel JF-20DX
Receiver group spacing	50 m
Receiver line distance	400–500 m
Recording system	Sercel 428 XL
Record length	5 s

Data acquisition was carried out by DMT Petrologic GmbH (Scholze and Wolf 2016a)

The first step was the conditioning of the input seismic data set, which was performed using Halliburtons software package SeisSpace ProMAX 3D®. The data quality was examined visually and with spectral analyses. Spectral balancing to boost higher frequencies was applied with care to preserve the amplitude behaviour proportional to the impedance contrasts, and to prevent noise amplification.

Furthermore, before performing the actual inversion workflow, a structural geological model was created as a constraint for the inversion. The structural modelling was carried out by Ziesch (2019) utilizing the software package SKUA-GOCAD by Paradigm. The 3D model contains 7 horizons (Top Aquitanian, Top Chattian, Top Rupelian, Top Priabonian, Top Berriasian/reservoir, Base Reservoir, and Top Callovian) and 24 faults (Figs. 3, 4). The horizons were first interpreted along inlines and crosslines at a spacing of 125 m with guided autotracking (using the maximum or minimum of the respective

Table 2 Overview of processing steps of the GRAME 3D seismic

Processing steps
Geometry setup
Zero phase transformation
Refraction static correction
Trace editing
Amplitude and divergence correction
Deconvolution
Iterative velocity analysis
Residual statics correction
CRS analysis
Iterative PreSDM velocity analysis based on PreSTM velocity field
RMO correction
Kirchhoff PreSDM
FXY deconvolution
Depthing

Data processing was carried out by DMT Petrologic GmbH (Scholze and Wolf 2016a, b)

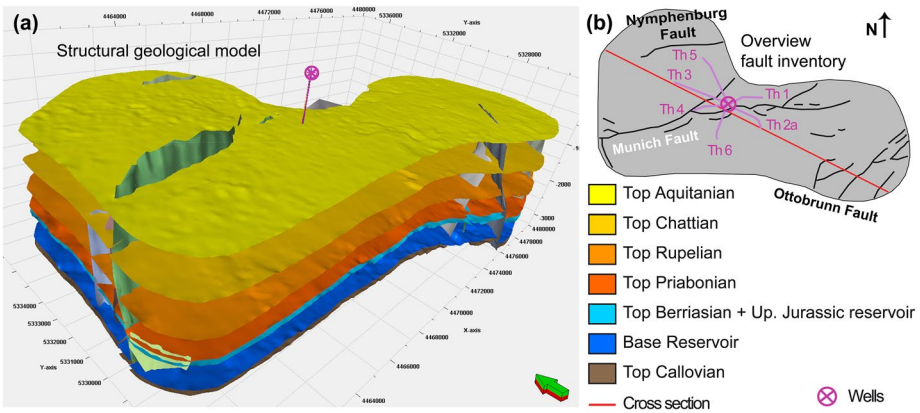

Fig. 3 Structural geological model of the Munich area with color-coded marker horizons based on the GRAME 3D seismic data set (**a**), and overview of the fault inventory and the well paths of the six Schäftlarnstraße boreholes Th1–Th6 (**b**). The cross section marked by the red line is shown in Fig. 4

phase) and then supplemented by 3D autotracking. The horizons itself were generated using the discrete smooth interpolation (DSI) algorithm, which allows the triangulated surface to be oriented as closely as possible to the interpreted point data set. Thus, preserving the morphology of the horizon surfaces. The interpretation of the faults was done manually. The fault sticks were interpreted in random lines perpendicular to the strike of the respective fault at a distance of 50 m. The surfaces of the faults were created by a direct triangulation of the interpreted point data sets and in a next step they were intersected with the horizons (Ziesch 2019).

In addition, the sonic logs (SWM 2019; Schölderle et al. 2021) were adjusted to meet the requirements for the seismic-well ties (correlation of the seismic data in time domain and the well data in depth domain). For the well log editing, the software package Well-CAD® was used. For all six wells (SLS Th1–SLS Th6) logging data were available, but not all measurements were conducted across the entire well path of all wells. For example,

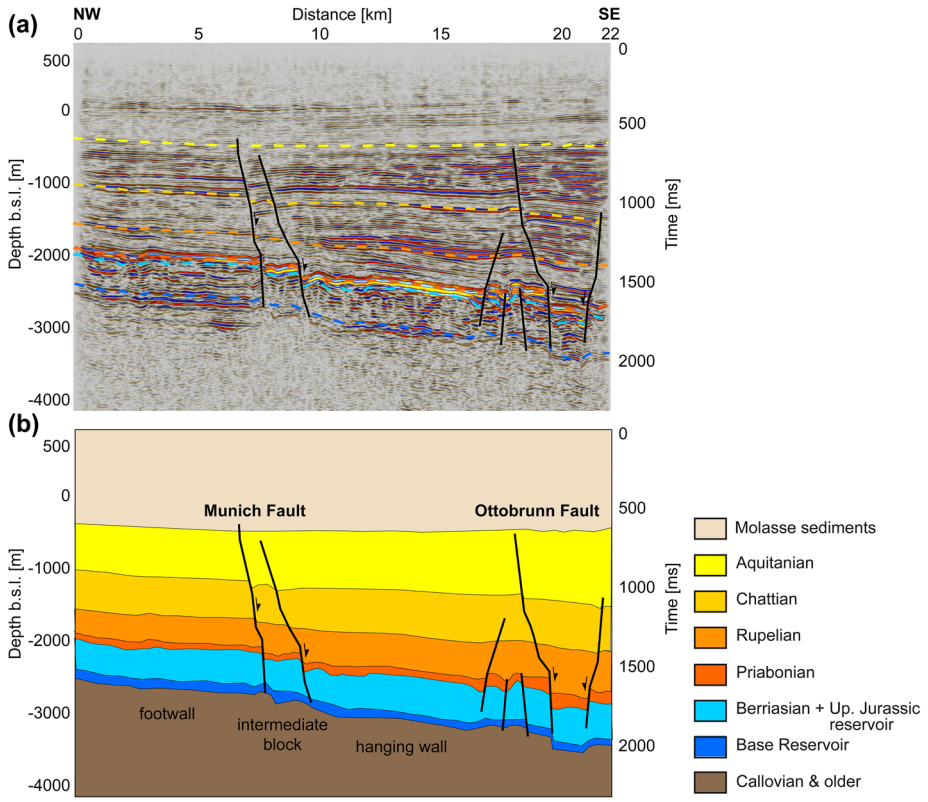

Fig. 4 Cross section through the GRAME 3D seismic intersecting the Munich Fault (**a**), and the corresponding geological interpretation (**b**). In the Schäftlarnstraße area the Munich Fault splits into two branches resulting in a three-part fault geometry which consists of a hanging wall, an intermediate block and a footwall

sonic logs were only measured for individual well sections. For all six wells a sonic log was carried out within section 4 which represents the reservoir (Fig. 5), but the uppermost section 1 was only measured in Th4, section 2 in Th1 and section 3 in Th4 and Th6. To get complete sonic logs the logs from the different sections were combined. For example, the combined sonic log for Th3 is composed as follows: for section 1 sonic log of Th4 + for section 2 sonic log of Th1 + for section 3 sonic log of Th4 + for section 4 sonic log of Th3. To generate synthetic traces for the seismic-well tie, a density log was also needed. Since no density log was measured, the sonic logs were used to calculate densities using Gardner's equation with individual lithology-dependent coefficients taken from literature (Mavko et al. 2009). For the later determination of a function to calculate the porosity from the acoustic impedance volume, porosity estimates were needed to be compared to impedance logs. The porosity estimates were calculated by the Technical University of Munich based on Archie's Law and verified and adjusted using porosity measurements from sidewall cores taken from two wells at the site SLS (Pfrang 2020).

The actual inversion workflow, for which the seismic interpretation software Schlumberger Petrel® was used, started with the seismic-well tie. For each well, the merged sonic log and the calculated density log were used to generate a synthetic trace in depth. This trace and the corresponding well tops, derived from lithology logs, were shifted to

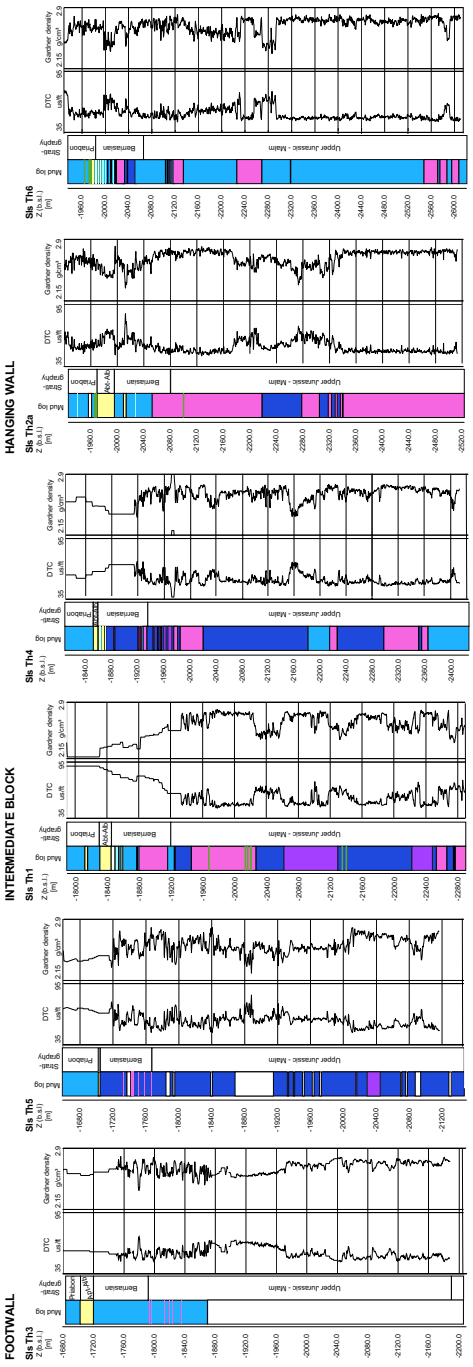

Fig. 5 Lithology (Böhm and Dax 2019), and sonic (Th1,Th2a,Th3,Th5 and Th6: SWM (2019); Th4: Schölderle et al. (2021)) and density logs of the six boreholes at the geothermal plant SLS drilled into the footwall, the intermediate block and the hanging wall of the Munich Fault. The sonic logs (DTC) were measured and the density logs were calculated using Gardner's equation. The geothermal reservoir is located in the Upper Jurassic Malm carbonates, mainly within Malm Zeta. In contrast to the wells drilled into the intermediate block and the hanging wall, the lithology of the reservoir could not be determined for the entire well path in the footwall due to heavy mud loss

match it to the reflectors of a seismic trace, extracted from the 3D seismic near the well paths, and the interpreted horizons in time (Fig. 6). The seismic-well tie was improved by visual examination and manual stretching and squeezing of the synthetic trace, generating a time-to-depth (TDR) curve for each well. The process was performed iteratively with a focus on the reservoir interval. Afterwards a wavelet was extracted for each well, and since only one wavelet can be implemented in the inversion, the six wavelets were combined to a zero-phase corrected mean-wavelet.

To run the inversion algorithm itself, a model grid was needed. This grid defines the geometry and the resolution of the inversion model. The resolution in x- and y-direction can be specified manually in metre-scale, while the resolution in the z-direction (the cell thickness) is determined automatically by the zone thickness. A zone is defined as the area between two horizons, but since this would result in a very poor vertical resolution, e.g., the zone between the Top Berriasian horizon and the Base Reservoir horizon has a height of about 600 m (or around 200 ms in time domain), the grid needs to be refined to get the optimal cell thickness. This was performed by creating additional layers in each zone. The layers were build along the stratigraphic thickness, which was measured perpendicular to the upper and lower horizon of each zone, with a proportional subdivision between the top and the base. Normally, one would prefer to follow

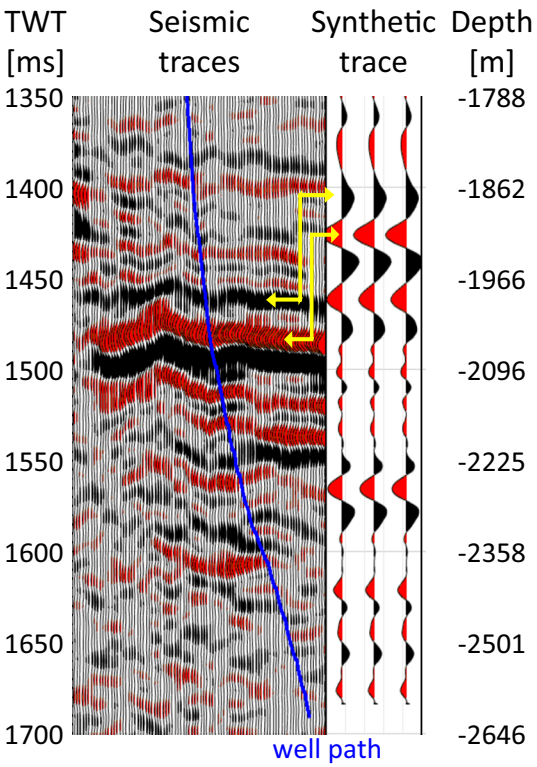

Fig. 6 Correlation of the seismic data in time domain (on the left) and the well data in depth domain (on the right), also called seismic-well tie. A synthetic trace derived from the sonic and density logs and the corresponding well tops, derived from a lithology log, were shifted to match it with the reflectors of a seismic trace, extracted from the 3D seismic near the well paths, and the interpreted horizons in time. The seismic-well tie was improved by visual examination and manual stretching and squeezing of the synthetic trace to extract a wavelet and to generate a time-to-depth (TDR) curve for the corresponding well

real geological layers, but the carbonate reservoir does not contain a continuous layering due to its depositional characteristics and the strong heterogeneity. Care was taken to ensure that the cell thickness is almost uniform throughout the model, but not so small that the calculation time for the inversion would become too long, e.g., in zone 4 (Priabonian) 20 layers and in zone 5 (Berriasian/Upper Jurassic carbonates) 100 layers were added. Afterwards the model grid was created based on the structural geological model with an x- and y-increment of 50 m (this corresponds to the resolution of the 3D seismic data set, which determines the horizontal resolution of the inversion) and a z-increment of around 2 ms (or around 6 m in depth domain; this value was chosen to accommodate the improved vertical resolution through the incorporation of the sonic logs).

The next step was an upscaling of the acoustic impedance logs (calculated from the merged sonic logs and the calculated density logs during the seismic-well tie) into the grid cells along the six well paths (Fig. 7). The upscaled data was then used to create a vertical mean trend as an input parameter to generate a trend model as a starting point for the inversion algorithm. For the horizontal trend, weighted surface attributes and properties were implemented, such as the velocity field and the reflection intensity.

This trend model was than used as an input parameter for the stochastic seismic inversion algorithm, together with the 3D seismic cube, the upscaled AI logs, and the estimated wavelet. Due to the good quality of the seismic data set, a convergence criterion of 0.7 with a maximum of 100 iterations was chosen. A value close to 1 implies that the optimization algorithm will search for a high match between the trend model and the real seismic data. Therefore, the inversion result will be more constrained by the seismic data than the trend model, although this leads to a longer computation time. After extensive parameter testing for a small number of realizations, a total number of 100 realizations was chosen for the final inversion. From these 100 models, an averaged model was calculated, which was than used for the interpretation of the acoustic impedance.

To convert the acoustic impedance model into a porosity model, a property relationship was determined. For that reason, a crossplot of the acoustic impedance logs and the porosity estimates from the six wells was generated (Fig. 8), and a linear function that describes this relationship was determined similar to other studies, e.g., Pendrel and Van Riel (1997); Dohlberg et al. (2000); Zeng (2012). By incorporating the data of all six wells the heterogeneity of the reservoir in terms of, e.g., lithology and facies distribution, and thus porosity distribution, can be better represented. Based on the linear function, in which low AI correlates with high porosity and high AI with low porosity (with a correlation coefficient of 0.75), the AI volume was converted into a porosity volume to describe the geothermal potential of the reservoir.

Results

For a better classification of the results and a better comparability with the drilling studies, a time-to-depth conversion was carried out for the acoustic impedance- and the porosity model. The main results are exemplarily and are shown as cross sections and depth slices through the acoustic impedance- and the porosity volumes. The plots show (a) features that were not or not in so much detail recognisable in the conventional reflection seismic, and (b) strong spatial variations of the reservoir properties. It has to

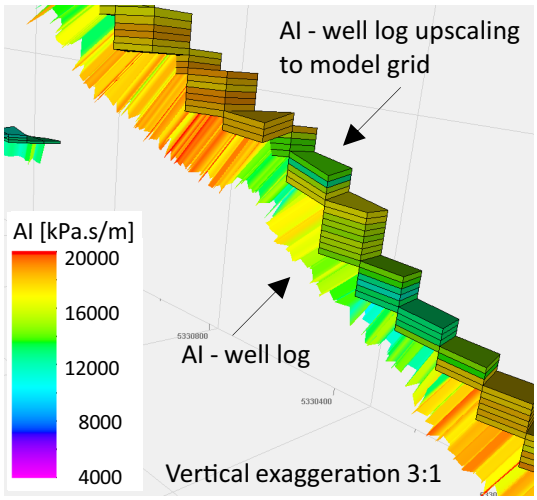

Fig. 7 The acoustic impedance logs (calculated from the sonic logs and the density logs during the seismic-well tie) were upscaled into the grid cells along the six well paths. The upscaled data was then used to create a vertical mean trend as an input parameter to generate a trend model as a starting point for the inversion algorithm

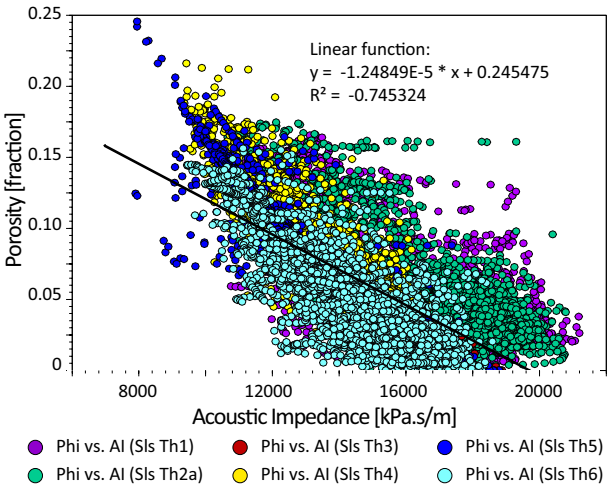

Fig. 8 Property relationship derived from a crossplot between acoustic impedance logs from the well-seismic tie carried out in this study and porosity calculations from sonic logs carried out by the Technical University of Munich (Pfrang 2020). With the linear function, the AI model from the inversion was converted into a porosity model of the reservoir

be noted that the porosity results are only valid for the zone between Top Priabonian and Base Reservoir, because only for that part porosity logs were calculated which were used to define a linear function (Fig. 8).

Inlines

NNW–SSE striking cross sections along inlines (IL) reveal spatial variations and features across different fault zones as outlined in Fig. 3b. IL 127 (Fig. 9a) is located in the western part of the study area crossing the Munich Fault between approximately crossline (XL)

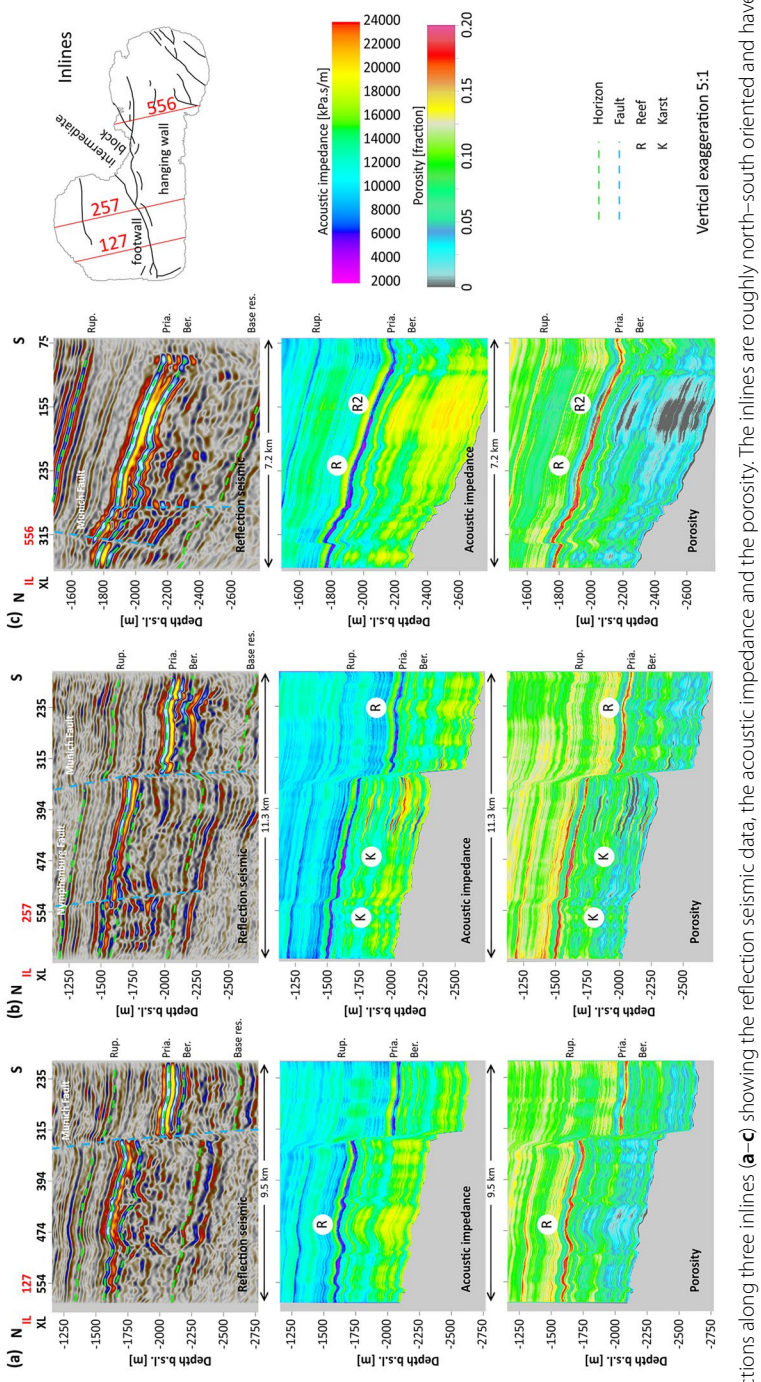

Fig. 9 Cross sections along three inlines (**a**–**c**) showing the reflection seismic data, the acoustic impedance and the porosity. The inlines are roughly north–south oriented and have a vertical exaggeration of 5:1. Reef R2 is the same a shown in Figs. 11 and 12. See text for interpretation

340 and 320. The continuous reflector at Top Priabonian typically has a very high amplitude due to the strong impedance contrast compared to the Rupelian formation above. The reflector at Top Berriasian (top reservoir) is also characterized as mostly continuous with a high amplitude but the contrast is less pronounced. At XL 474, the Berriasian reflector bends into a mound-shaped form with a diameter of 1.9 km. Internally the carbonate reservoir north of the Munich Fault is characterized by incoherent and chaotic reflections with low-to-moderate amplitudes in the upper and middle part and almost transparent areas in the lower parts. In contrast, the reservoir south of the Munich Fault features subparallel reflectors with moderate amplitudes. In carbonate rocks, a mound-shaped reflector with semi- to discontinuous reflections directly below is often associated with the upper part of a carbonate reef buildup. Transparent to chaotic reflections below these zones are expressions of the reef core (Burgess et al. 2013; Słonka and Krzywiec 2020). Parallel to subparallel reflectors in the south are interpreted as a bedded carbonate facies (Burgess et al. 2013; Słonka and Krzywiec 2020). The acoustic impedance (AI) from the inversion delivers a much more detailed image of the subsurface compared to the reflection seismic shown in Figs. 9 and 10. Therefore, the bedded facies in the south and also the implied reef are more pronounced and better imaged in the AI data. The reef geometry is imaged in more detail, e.g., showing the reef core, the reef slopes and the reef cap. The upper half of the reservoir shows generally slightly lower AI values than the lower half. With regard to the reef buildup, the upper part of the reef has AI values between 10,000 and 18,000 kPa s/m and the lower part ranges between approximately 15,000 and 20,000 kPa s/m. By taking the calculated porosities into account, the identified features can also be described qualitatively. With regard to the reef structure, the core has porosities between 0 and 3% in the lower part and 1 to 4% in the upper part, with a region of high porosity of 6 to 9% in between these zones. In the reef cap and on the slopes, increased porosities with 7 to 12% are observed. Overall, the porosity is higher in the upper half of the reservoir compared to the lower half.

IL 257 (Fig. 9b) is situated in the central part of the study area, crossing the Munich Fault in the south between XL 355 and XL 335. Again, the Top Priabonian is marked by a distinctive high-amplitude reflector that can be observed across the entire GRAME 3D seismic data set. The reflector marking Top Berriasian looks more disrupted compared to IL 127, especially north of the Munich Fault, and to the south at XL 235, it forms a small upward bending structure 700 m in diameter. This structure is interpreted as the upper part of a small reef. The carbonate reservoir itself is characterized by parallel reflectors with high to moderate amplitudes in the northernmost part, disrupted subparallel reflectors with low to transparent amplitudes in the middle part (between the Nymphenburg- and the Munich Fault), and disrupted chaotic reflectors south of the Munich Fault with transparent areas in the lower part of the reservoir. The parallel reflectors are interpreted as a bedded carbonate facies and the disruptions and partly low amplitude areas, particularly in the upper third of the reservoir, might be indicators of karstification due to dissolution along, e.g., bedding planes and fractures. The AI shows values between 12,000 and 18,000 kPa.s/m for the upper part of the small reef in the south and values ranging from 15,000 to 19,000 kPa.s/m in the lower part. The zones with presumed karstification are characterized by mostly low AI values, e.g., at XL 474 between −1700 and −1900 m depth. Overall, except for some anomalies (< 7000 kPa

s/m and > 20,000 kPa s/m) close to the Munich Fault, the AI is slightly lower on the footwall than on the hanging wall. The seismically almost transparent areas in the central upper part of the carbonate succession, with presumed karstification, have porosities around 10 to 12%. In this area north of the Munich Fault even the lower half of the reservoir has quite high porosities with up to 8% compared to the surrounding regions. The small reef in the south has low porosities (0–4.5%) in the core and high porosities of 6.5 to 11% at the reef top, the slopes and in the central part between −2260 and −2340 m depth.

IL 556 (Fig. 9c) is in the eastern part of the GRAME area. Both the Top Priabonian and the Top Berriasian have continuous high-amplitude reflectors. In the north, where the inline crosses the branches of the Munich Fault, parallel patterns revealing a bedded facies are observed. To the south, the upper part of the reservoir consists of mound-shaped, hummocky patterns, whereas the lower part is characterized by chaotic to transparent reflection patterns. Thus indicating massive facies with a reef build up of 2 km diameter at XL 155. This reef is also observable in the AI data. Directly adjacent to the north another reef with a lower AI and undulating surfaces in the upper half is imaged, although it is possible that these features are part of one large reef (stretching from XL 260 to XL 115). The different appearance in the north and south may be caused by karst processes occurring close to the fault forming an undulating surface on the northern side due to dissolution induced subsidence and sinkhole development. This assumption is in agreement with the porosity model that reveals higher porosities of 5 to 15.5% in the north, especially in the upper part of the reef, compared to the south with porosities of around 0 to 8%. The highest porosities are found in the undulating surface at the top of the reservoir close to the fault.

Crosslines

Cross sections along crosslines show spatial variations and features in a rough west–east direction running parallel to the Munich Fault. XL 143 (Fig. 10a) is located in the south of the study area, crossing the Ottobrunn Fault in the eastern part. The carbonate reservoir shows a mainly chaotic and transparent reflection pattern indicating massive facies. At the uppermost part of the reservoir two mound-shaped structures, interpreted as reefs, with diameters of 2 km and 1.6 km are observed at IL 560 and IL 750, respectively. Furthermore, a wide depression at IL 720 with a width of 700 m and a smaller indentation truncating the underlying deposits at IL 635 with a width of 300 m are observed and both are assumed to be the result of carbonate dissolution leading to the formation of local sagging sinkholes and collapse sinkholes (Gutiérrez et al. 2008). In addition to the two reefs identified in the reflection seismic data, a third one with 1.5 km width can be seen in the AI data at XL 670. The reef cores, especially in the lower parts, have high AI values, while the reef cap and also the slope areas show much lower values. The two identified dissolution-induced sagging and collapse structures at IL 635 and IL 720 are located above the slopes of the third reef. In contrast to the reflection seismic data, these features are more clearly visible in the AI data. For example, the indentation at IL 635, probably a sinkhole, has not only truncated the underlying deposits, but the overlying deposits also appear to be falling or bending into this collapse. Since the Priabonian

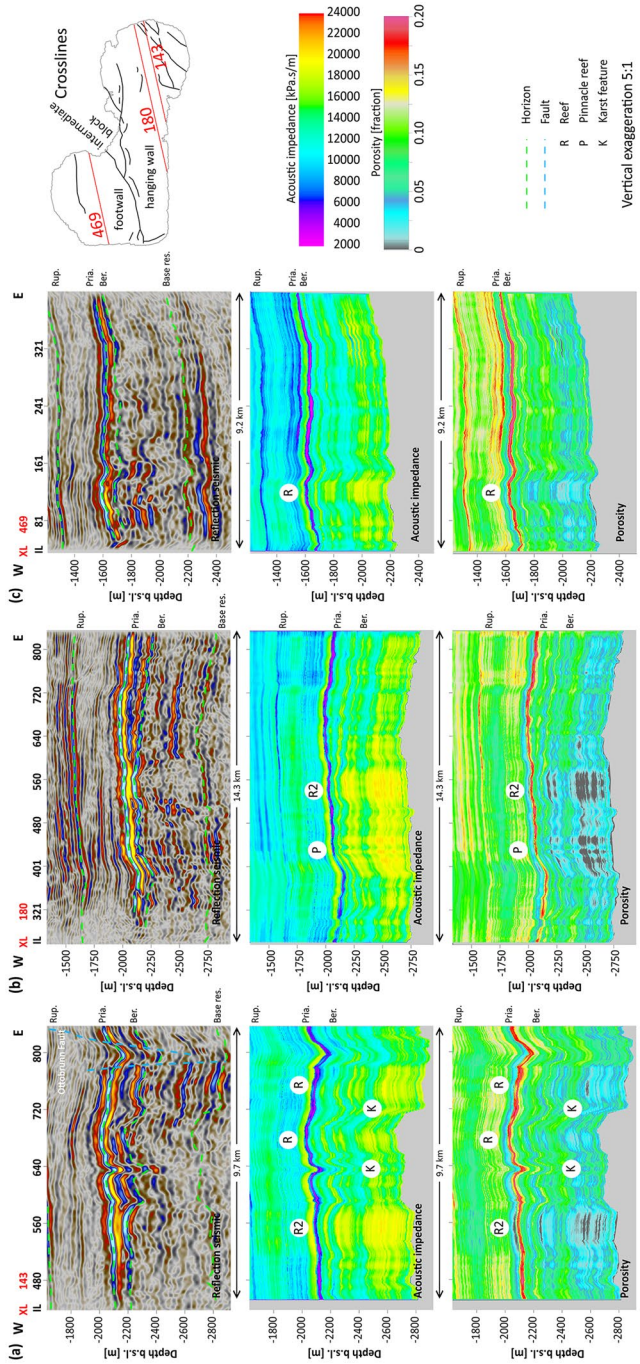

Fig. 10 Cross sections along three crosslines (**a**–**c**) showing the reflection seismic data, the acoustic impedance and the porosity. The crosslines are roughly west–east oriented and have a vertical exaggeration of 5:1. Reef R2 is the same a shown in Figs. 11 and 12. See text for interpretation

and the lower part of the Rupelian are also affected, it seems that the actual collapse event happened after deposition of these overlying materials, perhaps during the time between Late Rupelian (Lower Oligocene) and Miocene. In contrast, the larger subsidence feature at IL 720 contains bending layers only in the reservoir and up to the middle of the Priabonian formation. Sagging must have started during the Upper Jurassic and declined over time until it ended during the Lower Cretaceous, thus allowing the Priabonian limestones to fill the depression. Both depressions show relatively low AI values between 8400 and 13,000 kPa.s/m. The corresponding porosities are quite high, with up to 13%, similar to other reef slope areas (e.g., at the reef in the west). The porosity distribution of the reefs varies from west to east. The western reef has much lower porosities in the upper part than the two reefs to the east.

XL 180 (Fig. 10b) is also situated in the south of the GRAME seismic. In contrast to XL 143 the carbonates show a subparallel, partly disrupted reflection pattern with high amplitudes in the western part. A transparent area with a mound-shaped Top Berriasian reflector (1.8 km width) is observed in the central part at IL 560, and to the east the upper section consists of incoherent and almost transparent reflections, whereas the lower section shows discontinuous parallel reflection patterns with low-to-moderate amplitudes. The western and eastern areas probably belong to the bedded facies, with a localized massive facies in the center in the form of a reef buildup. This interpretation is in agreement with the inversion-derived AI results. In the eastern part a layered zone in the carbonate reservoir can be identified with several layers showing high AI values of 16,000 to 18,000 kPa.s/m. The reef in the center is also clearly visible and a second one to the west at IL 435 with a diameter of 1.2 km is also observed. In contrast to the first reef, the second is characterized by a strongly undulating surface forming notch-shaped buildups that can be interpreted as pinnacle reefs. These pinnacles have low porosities (0–3.5%) in the core and higher porosities (5–10%) at the top and the small flanks. In general the reefs have low porosities except for the slopes, the top and a larger area in the center between −2300 and −2400 m depth and IL 456 and IL 526. The bedded facies to the east is characterized by mostly moderate porosities and a few high porosity layers of 10 to 13%.

XL 469 (Fig. 10c) is in the northern part of the study area on the footwall of the Munich Fault. In contrast to the crosslines on the hanging wall, the Top Berriasian is a discontinuous reflector that almost vanishes in the central part between IL 180 and IL 300, which might be a result of intensified karstification. Internally, except for the western area with some strong parallel reflectors, the carbonates of this crossline show a subparallel to hummocky, almost transparent, reflection pattern in the upper half of the carbonate reservoir, and parallel reflections with low-to-moderate amplitudes in the lower half. By just taking the conventional reflection seismic data into account it is not clear if this area belongs to the bedded facies, modified by strong dissolution along bedding planes, or to the massive facies. The acoustic impedance reveals a 1.4 km wide mound-shaped structure in the west at IL 120 that is interpreted as a reef (massive facies) with high AI values in the core and lower values of 10,000 to 13,000 kPa s/m on the slopes. To the east, a weak disturbed layering (bedded facies) can be observed in the upper half of the reservoir with quite low AI values ranging from 9000 to 16,000 kPa s/m. The corresponding

porosity model indicates a few layers with porosities of 12 to 13%, which might be the result of dissolution and, therefore, increased secondary porosity along bedding planes. The reef is smaller in diameter and has slightly higher porosities compared to the ones located on the hanging wall as observed in the other cross sections.

Depth slices

For a better understanding of the porosity distribution across the reservoir, the model was also interpreted using depth slices, which capture the horizontal variations for a given depth (Fig. 11). At −1682 m depth the zone between Top Priabonian and base reservoir is only found in the footwall of the Munich Fault due to the fault-controlled downward stepping of formations to the south. As already shown by the cross sections, the reservoir in the footwall is characterized by relative high porosity values with the highest values (10 to 13.5%) located in the northwest and in the southeast near boreholes SLS Th3 and Th5. Furthermore, in these areas clusters of circular features can be seen, which are interpreted as dissolution-induced sinkholes or sagging structures. These karst elements have high porosities at their edges (e.g., 13%), and lower porosities in their center (e.g., 8%). At −1784 m depth, three other circular karst features are observed in the west on the footwall block and also a reef with a diameter of 1.5 km. At −1816 m depth, a second reef is identified to the west in the footwall of the Munich Fault, which can also be seen on IL 127 and XL 469. Besides that, two circular structures, interpreted as karst-related sinkholes or sags are located to the east of the intermediate block with porosities ranging from 8.5% in the center to 13.5% on the edges. Other sinkholes are observed in the intermediate block or close to it at a depth of −1877 m. Moreover, in the northern part of the hanging wall, two other sinkholes can be clearly seen and a large reef that is also observable at greater depths and is shown in detail in Fig. 12. At −1930 m depth, a small circular structure, a sinkhole or a sag, is seen on top of the reef. At −2052 m and −2105 m depth, sinkholes are identified along the Munich Fault and the Ottobrunn Fault, showing strongly varying porosities as low as 3% in the center and as high as 18% on the edges. Furthermore, at −2105 m and −2195 m depth, several reefs are observed to the south of the hanging wall, which can also be seen in cross sections IL 257, IL 556, and XL 180. Other smaller reefs are identified at −2406 m in the Ottobrunn Fault Zone. In general, the footwall and the intermediate block of the Munich Fault show relatively high porosities, whereas the hanging wall shows relatively low porosities with decreasing values from west to east.

3D view of reefs and sinkholes

In Fig. 12, detailed illustrations of reef buildups, a sinkhole and karst along bedding planes are shown in a 3D view. The reef buildups (Fig. 12a, b, e) show intensive vertical (aggradational) and lateral (progradational) growth due to sea level changes, especially a rising sea level, that resulted in the development of large reef complexes. These reefs have a complex porosity distribution. The reef core has mostly low porosities of 1 to 3.5% and at the reef base, porosities < 1% are observed. However, even within the core, areas can be found with higher values of up to 8%. The highest porosities of up to 14% are observed in the reef cap, in the upper third of the reef and especially towards the edges at the reef slopes. At the slopes, a characteristic interfingering of

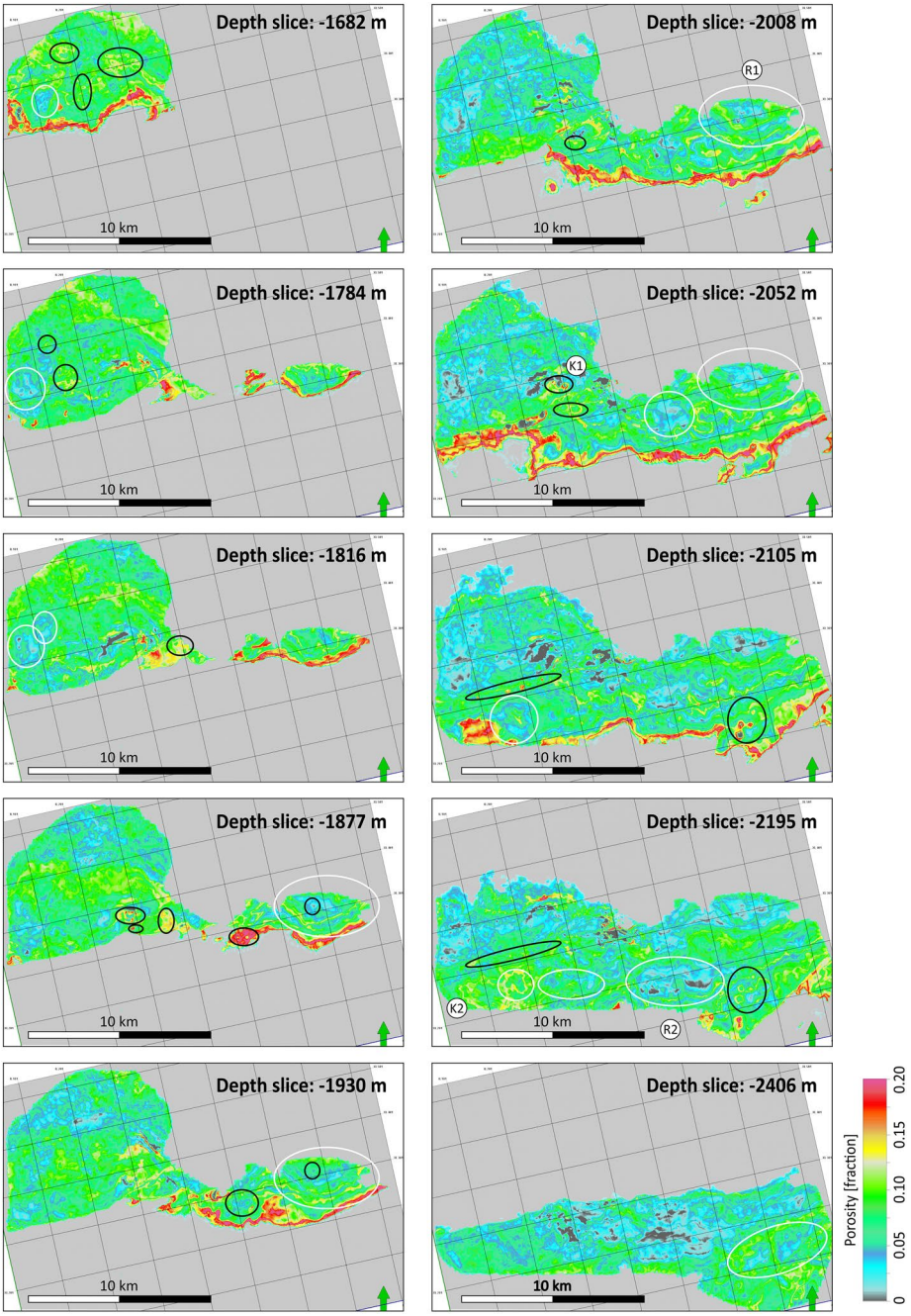

Fig. 11 Depth slices through the porosity model. Only the areas between Top Priabonian and Base reservoir are shown, the other zones such as the Chattian are hidden. Reef buildups are marked by white circles (reefs R1 and R2 are shown in detail in Fig. 12a, b) and karst features by black circles (karst features K1 and K2 are shown in detail in Fig. 12c, d). See text for interpretation

the reef facies with the surrounding strata, in the form of rounded pine tree shaped edges, can be seen. This development of an interfingering strata results from sea-level changes that caused the shoreline to migrate back and forth, indicating a syn-sedimentary reef development with slightly varying build up growth rates. Within the high porosity zones, undulating surfaces or large depressions and collapse structures

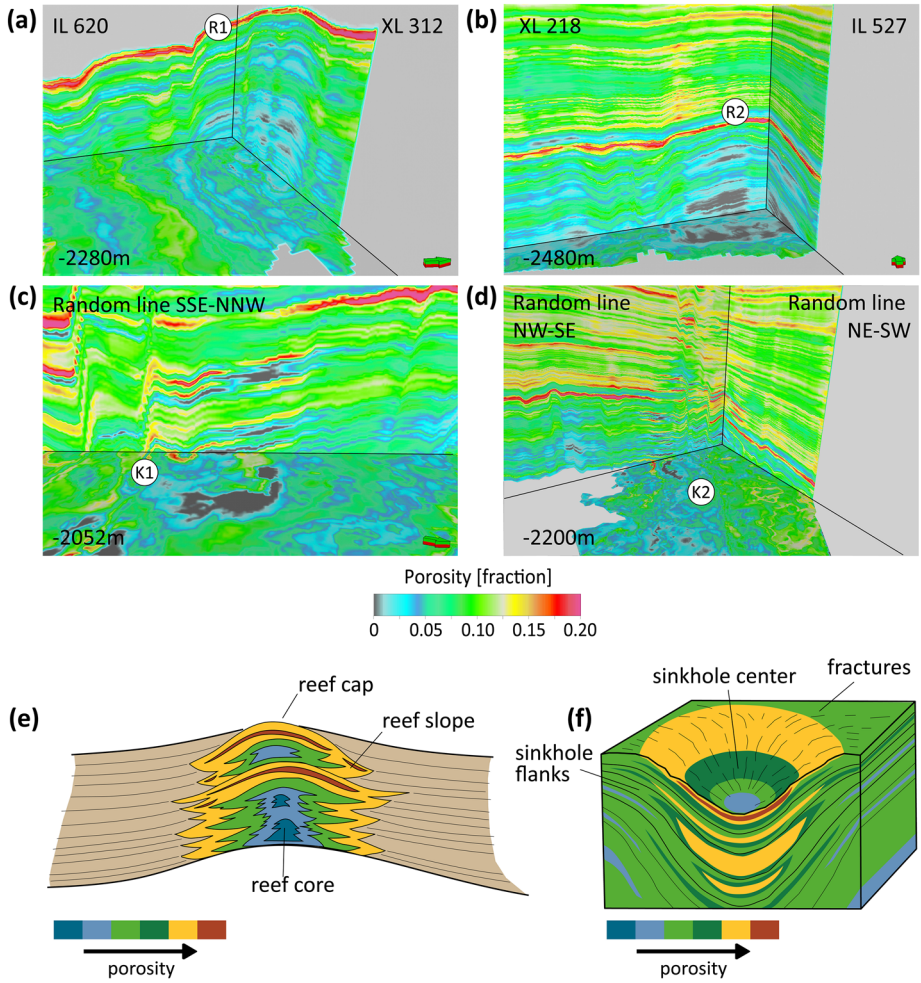

Fig. 12 Detailed view of the porosity model showing reef buildups (**a**, **b**), sinkholes (**c**) and karst along bedding planes (**d**). The vertical exaggeration is 5:1. (**e**) Sketch showing the structure and porosity distribution across a reef buildup with lower porosities in the reef core and higher porosities at the slopes and the reef cap, and (**f**) porosity variations across a karst sinkhole. See text for interpretation

can be seen that are interpreted as sags and sinkholes induced by intensified carbonate dissolution which goes along with increased secondary porosity. A detailed image of a sinkhole and the corresponding porosity distribution is shown in Fig. 12c and f. Sinkholes are visible as circular structures located in dissolvable rocks. Sinkhole edges show porosities of up to 18.3%, which is very high even compared to the reef slopes, whereas, the sinkhole center is characterized by low values and the overlying material falling or bending into the void. Carbonate dissolution does not always form such distinct features, such as sags and sinkholes. Sometimes it can also appear along bedding planes leading to increased secondary porosities (Fig. 12d). This type of high porosity zone can stretch across large areas.

Lithology-dependent porosity analysis

Porosity histograms (Fig. 13) for the reservoir zone reveal a wide range of porosity values which result from strong heterogeneity of the carbonates. For the entire model the

porosities range from 0 to around 20% and for the areas along the wells, a range between 0 and 14% can be observed. Figure 13 shows porosities within the different lithologies along the drill paths. The histograms reveal that, in order of decreasing porosity, the dolomitic limestone has the highest porosities, followed by pure limestone and pure dolomite, and the calcareous dolomite has the lowest porosities within the carbonate reservoir.

Discussion

A significant aspect of reservoir characterization in carbonates is the fact that it is much more complicated than in sandstones. Carbonates are more complex due to diagenetic overprints, karstification, fracturing and the formation of reef buildups (Fig. 14a–k). Thus, the carbonate rocks are typically heterogeneous regarding porosity and permeability distribution (Ehrenberg and Nadeau 2005; Lucia 2007; Ghafoori et al. 2009). In the following section the diagenetic processes that have influenced carbonate reservoir

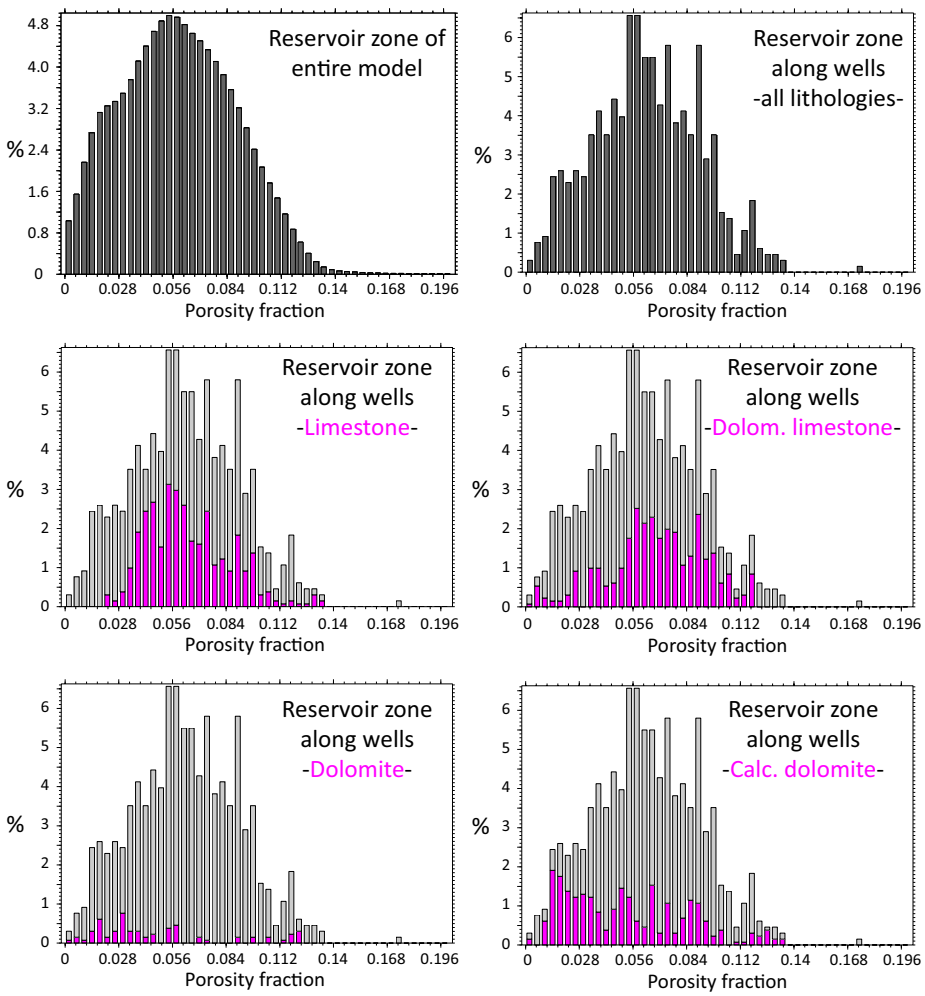

Fig. 13 Porosity histograms of the reservoir zone for the entire model and along the drilling paths derived from the inversion results. The wide range of porosity values results from the strong heterogeneity of the carbonates due to effect of different processes on the pore space, such as dolomitization, cementation and dissolution. Overall, the dolomitic limestone shows the highest porosities and the calcareous dolomite the lowest

porosity in the greater Munich area will be examined, the porosity distribution trends and the reservoir quality will be discussed and the methodological approach will be inspected.

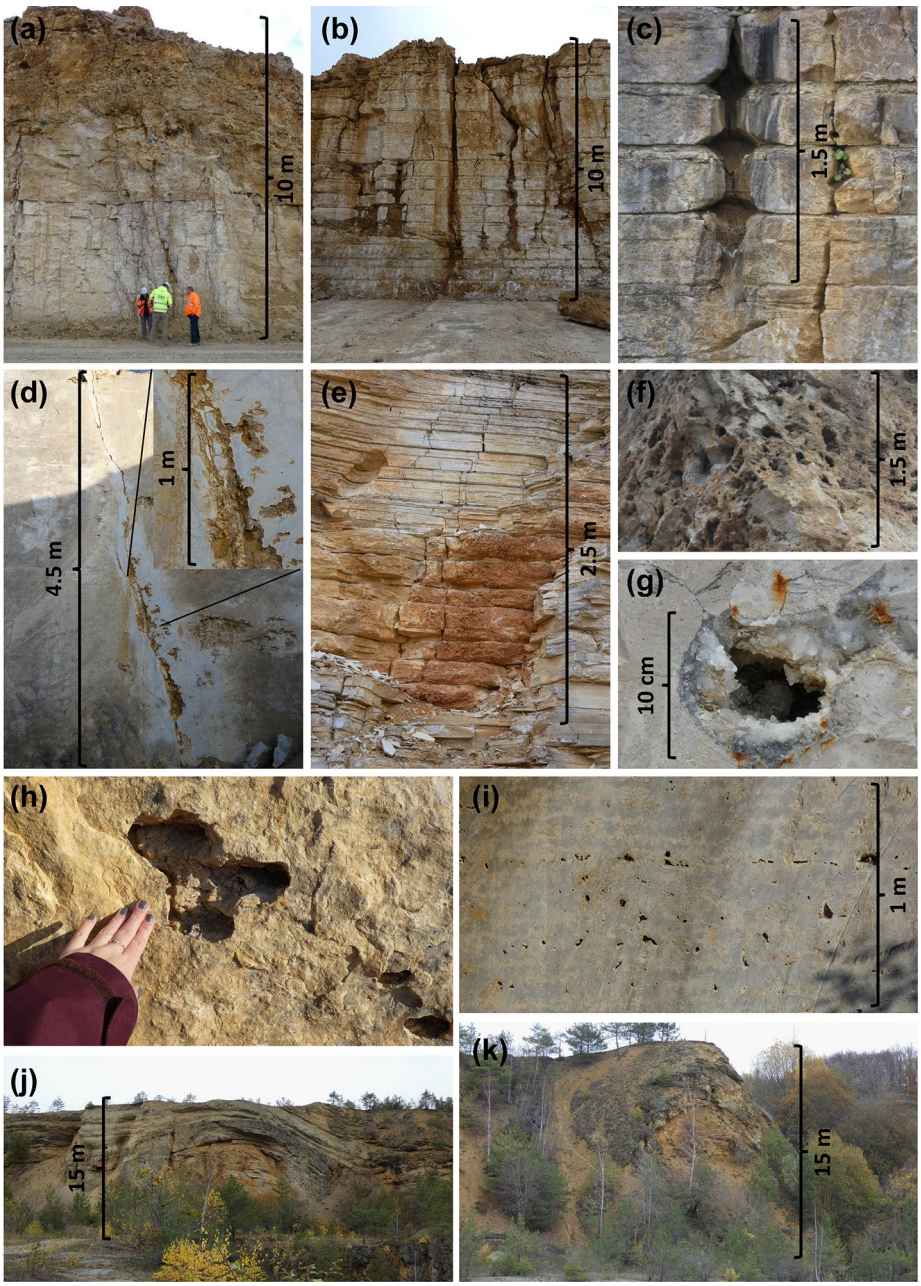

Fig. 14 Outcrop photos of the Jurassic carbonates from the Franconian Alb (**a**) showing dissolution along fractures (**b**–**e**), intense karstification of massive facies (**f**–**h**) and along bedding planes (**i**), with cavities partly cemented by calcite (**g**), and reef buildups (**j**, **k**). Karst and fractures are the most important controlling factors of the reservoir quality in the research area, but the irregular distribution of karstified and fractured zones makes it necessary to analyse it in 3D using, e.g., seismic methods

Diagenetic processes

The most important diagenetic processes affecting the porosity in carbonates are cementation, compaction, dolomitization, and dissolution (Ghafoori et al. 2009). Cementation is a main reason for porosity reduction in carbonates. With increasing burial depths and temperatures the solubility of $CaCO_3$ declines, leading to the precipitation of, e.g., calcite that can clog or seal both primary and secondary porosity. This can be observed in outcrop analogues from the Franconian Alb, where the Jurassic carbonates crop out (Fig. 14g) and has been proven by laboratory investigations of rock probes from the Jurassic carbonates (Wolfgramm et al. 2011; Homuth 2014). Another porosity reducing process is compaction due to increasing burial depths. For depths of around 2 km, limestone and dolomitic limestone are presumed to be more porous than dolomites, and at greater depths dolomites are more porous and permeable than limestones according to a study carried out in Florida (Schmoker and Halley 1982). In the Munich area, the reservoir is located deeper than 2 km depth, but the highest porosities are still found in the dolomitic limestone and the dolomites show the lowest porosities (Fig. 13). This shows that no generalized statement about the porosity–depth relationship with regard to the different lithology types can be made for our study area. During dolomitization calcite is replaced by dolomite leading to a reduction of the rock volume and, therefore, an increase of the total porosity by creating secondary porosity (Sajed and Glover 2020). Furthermore, early dolomitization can preserve primary porosity by creating a stable framework which hampers compaction (Lucia 2007). This often results in a more heterogeneous distribution of petrophysical properties (Ehrenberg and Nadeau 2005; Ehrenberg 2006) and it can lead to a redistribution of the pore space, e.g., in the Leduc reef carbonates in Alberta (Mountjoy and Marquez 1997). The percolation of unsaturated water can lead to the dissolution of calcite or aragonite, and the formation of secondary porosity and even large cavities, sinkholes and sagging structures (Kendall and Schlager 1981; Xu et al. 2017), as it is observed in the Franconian Alb (Fig. 14f–i) and in the Malm carbonates of the Munich area. This is the most important process that increases reservoir potential. Due to these many and complex processes affecting the porosity of carbonate rocks, the final porosity may not be related to the original depositional environment at all.

With respect to the German Molasse Basin and the associated carbonate platforms, the petrophysical and hydraulic properties of the Malm aquifer are very heterogeneous due to the variability of depositional and diagenetic features, karstification, fractures, and faults (Koch 2000; Mraz 2019; Bohnsack et al. 2020). In our study area, these features led to the formation of a dual porosity reservoir mainly affected by karst and fractures (Fig. 14). Both are important controlling factors of the reservoir quality and they also have an influence on permeability which varies according to, e.g., fracture type, -intensity, -orientation and -distribution, and karstification intensity (Konrad et al. 2019; Bohnsack et al. 2020; Sajed and Glover 2020). For example, the fracture orientation in relation to the maximum horizontal stress field (SH_{max}) may have an influence on whether the fractures are open or closed (Cacace et al. 2013). The strong variability of porosity and permeability, due the irregular distribution of karstified and fractured zones, pose a problem for geothermal reservoir characterization, e.g., prediction of hydraulically active zones.

Porosity distribution

In general porosity of carbonates can vary from almost 0% in tightly cemented rocks to about 35% in unconsolidated sediments (Lucia 2007). Log analysis from Moosburg and Dingolfing in the GMB revealed porosity ranges of 1.0 to 24.0% for the Malm (Bohnsack et al. 2020); a similar range of 0.0 to 20.0% is also observed in our study area in Munich (Fig. 13). At Moosburg and Dingolfing high porosities correlate with karstified zones, vuggy layers or bioturbation based on image log interpretations. In addition, gamma ray logs show very heterogeneous deposits in the upper part of the reservoir and more uniform sediments in the lower part based on a study by Bohnsack et al. (2020). Furthermore, they showed that the Upper Jurassic formation can be subdivided into the three porosity units, Malm ζ (0.3 to 19.2% – median 4.8%), Malm ϵ–δ (0.5 to 12.2% – median 2.9%), and Malm γ–α (0.3 to 3.5% – median 1.7%) (Bohnsack et al. 2020). This porosity distribution corresponds with the results of this study in which the lowest porosity values are found in the lower most part of the Malm carbonates. Therefore, we interpret it as a zone of poor potential for geothermal exploitation due to unsuitable porosity conditions. In the middle depth range, the carbonates below Munich have mostly low porosities except for zones affected by, e.g., dolomitization (as observed in the SLS boreholes), karstification (visible in the SLS boreholes and the GRAME 3D seismic) and reef buildups (identified by the seismic inversion), thus improving hydraulic connectivity. The highest porosity values are located in the upper part of the carbonate succession, which is consistent with the results of Böhm (2012) and Böhm et al. (2013).

The spatial variability of porosity in the Munich area results from the heterogeneity of the lithology types, the different diagenetic processes described above, and varying karstification intensity. The spatial porosity distribution seems to follow a trend as observed in the inversion results with higher porosities and more intense karstification to the north of Munich compared to the south (Fig. 15). This is indicated by the presence of numerous sinkholes identified in the reflection seismic data and by circular structures with low impedance and, therefore, high porosity as indicated by the inversion results. The low impedance values within the sinkholes are supported by the modelling results from Sell et al. (2019) for the GRAME area, who showed that seismic velocities decrease in the sinkhole center compared to the surrounding or overlying material. Furthermore, we show that the sinkholes form local clusters within the footwall of the Munich Fault and along the faults. Carbonate dissolution can also occur along bedding planes, without forming sinkholes, which can lead to increased secondary porosities that can stretch across large areas. The dissolution within the massive facies and along bedding planes in the bedded facies can form disrupted and vuggy layers which are observable as discontinuous reflectors and/or undulating reflectors in the 3D seismic. In these areas the top of the carbonate reservoir formation is often characterized by low seismic amplitudes, because the leaching of the carbonates significantly reduces the original high impedance contrast with the overlying rocks. Furthermore, the generation of many small-scale features such as cavities created by dissolution or fractures induced by local stress redistribution due to collapsing cavities, can lead to increased scattering of the seismic waves which results in a loss of reflected energy and, therefore, reduced seismic amplitudes. The more intense karstification of massive, but also bedded carbonate facies north of Munich and the resulting higher transmissivity was also observed by Birner et al. (2012),

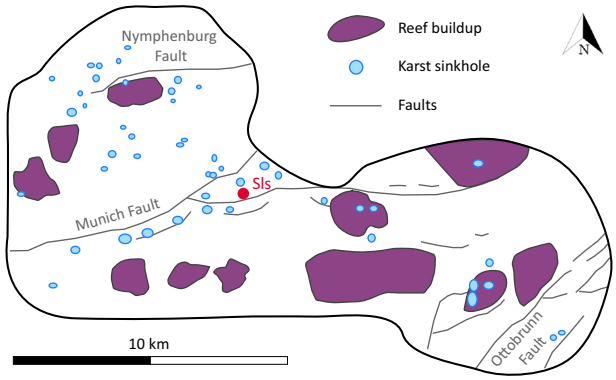

Fig. 15 Distribution of reef buildups and karst sinkholes across the GRAME study area below Munich. Karstification is more intense to the north and larger and better pronounced reef buildups are found in the south

who investigated the hydraulic parameters of the Upper Jurassic aquifer with respect to it's potential for geothermal exploitation. We assume the reason for the intense karstification to the north are the more widespread higher (secondary) porosities combined with a higher permeability due to fractures and a better connected porosity. The higher permeability allowed intensified circulation of unsaturated waters which dissolved large rock volumes, removed the dissolved material and formed new secondary pore space and cavities. Over time new fractures can form in the surrounding areas of cavities due to collaps and local stress redistribution. These fractures can serve as additional fluid pathways for unsaturated water leading to self-reinforced carbonate dissolution. The typically strong fracturing around faults and, therefore, often enhanced permeability is also the presumed reason for the accumulation of sinkholes along the Munich- and the Ottobrunn Fault. Similar observations for enhanced dissolution of soluble rocks close to faults were made by Abelson et al. (2003); Closson and Abou Karaki (2009); Wadas et al. (2017) and Wadas et al. (2018).

Besides karst structures, we also identified carbonate reef buildups in our study area, which are associated with massive facies, e.g., microbial–sponge buildups, and they often pass laterally into the surrounding bedded facies (Słonka and Krzywiec 2020). They are favoured targets for reservoir exploitation, but commonly they are very complex regarding the distribution of petrophysical parameters and facies. Often the reef core is described as a good exploitation target, but this is not always the case as demonstrated by Słonka and Krzywiec (2020) and this study. We show that the reef caps and reef slopes have increased porosities with around 7 to 14% and the reef cores have low porosities of mostly < 3%. We assume that this is the result of intense karstification and gravitational mass flows on the slopes. The reef slopes show a characteristic interfingering of the reef facies with the surrounding strata, in the form of rounded pine tree shaped edges, which indicates a syn-sedimentary reef development with slightly varying build up growth rates. The same was observed by Słonka and Krzywiec (2020) for the Miechów Trough in Poland using well data and 2D seismic lines. Buildups can appear as either continuous elongate bodies oriented parallel to the shelf edge or isolated structures, where the reef geometries are affected by sea level changes and the accommodation space produced by regional subsidence (Moore 2001). In the Munich area, it seems that the reefs are

roughly oriented parallel to the former passive Tethys margin and, therefore, the Franconian Alb striking W–E to SW–NE at this location. Furthermore, the reefs seem to be larger and better pronounced south of Munich compared to the north (Fig. 15). However, this interpretation mirrors only the results for the GRAME 3D seismic area and on a larger scale there might not necessarily be a preferred orientation of the reef structures. This preferential reef orientation can only be proven by analysing other 3D seismic data sets of the GMB. In addition to the typical large-scale ($\sim$ > 1 km diameter) buildups we also identified small notch-like reefs on top of a larger complex, which we interpreted as pinnacle reefs. Pinnacles are formed by so called frame builders, while normal reef build ups consist of accumulated lime silt, mud, sponges, algae and crinoids. In the case of a very fast rising sea level, pinnacles can be formed locally in areas, where the carbonate production can keep pace. Both pinnacle reefs and reef buildups are formed on local highs due to the presence of karst topography or other surface irregularities, and seaward build ups contain more porous grainstones (grain-supported carbonate rocks that contain less than 1% mud-grade material) than shelfward buildups. Cementation is also greater seaward causing a decrease in porosity (Moore 2001). The Munich area was located in a shallow marine environment with probably less porous grainstones and less cementation, but still displays a complex porosity distribution throughout the carbonate reservoir.

Reservoir quality

In general, the cut-off porosity for most carbonate reservoirs is 3%, compared to 8% for sandstones (e.g., Tiab and Donaldson 2015; Mehrabi et al. 2019). Based on this assumption and the observed porosity ranges, we define porosity evaluation levels for estimation of reservoir quality as follows: 0 to 3% are negligible, 3 to 6% is poor reservoir quality, 6 to 9% is moderate, 9 to 12% is defined as a good reservoir, and > 12% is a very good reservoir quality. As described above, the porosity values show a strong difference between the upper part and the lower part of the carbonate reservoir. Therefore, we subdivided the Malm reservoir into three units similar to Bohnsack et al. (2020), based on the sequence stratigraphic interpretation for the geothermal site SLS by Wolpert et al. (2020), and created average porosity maps for each unit to define areas with high and low reservoir quality (Fig. 16). Note that the values at the far edge of the model are influenced by edge effects during modelling and should be neglected. For the first unit, Berriasian to Malm ζ4, almost all areas have a moderate to good reservoir quality, especially the northern and northeastern parts of the footwall of the Munich Fault and the southwestern part of the hanging wall due to increased secondary porosity as a result of intensified karstification as shown by several large sinkholes, sinkhole clusters and widespread dissolution along bedding planes. Further areas with good reservoir quality are found on the intermediate block of the Munich Fault and along the deformation zones of the Munich Fault and the Ottobrunn Fault. For the second unit, Malm ζ3 to Malm ζ1, the only large areas with moderate reservoir quality are found on the footwall block, except for the most western area, and on the hanging wall block west of the Munich Fault. The east of the hanging wall and the area around the Ottobrunn Fault show a mixture between poor and moderate quality. A larger area with negligible reservoir porosity is located in the central part of the hanging wall, where larger reef buildups with low

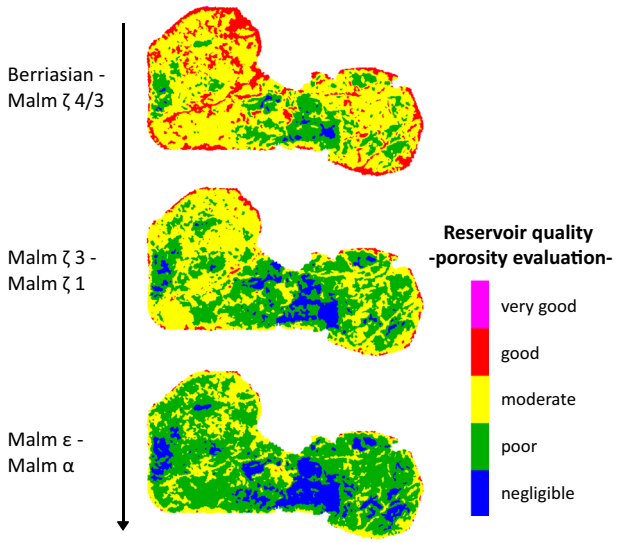

Fig. 16 Map view of reservoir quality based on porosity evaluation for three different zones: Berriasian to Malm ζ4/3, Malm ζ3 to Malm ζ1, and Malm ε to Malm α. The stratigraphic subdivision is based on the sequence stratigraphic interpretation for the geothermal site SLS by Wolpert et al. (2020). It has to be noted that this reservoir quality estimation is just based on a porosity evaluation and no permeability values are included. According to Homuth (2014), Bohnsack et al. (2020) and Moeck et al. (2020), not only porosity, but also permeability in the GMB is characterized by strong heterogeneity, and they have shown that no general trend describing the porosity–permeability relationship based on stratigraphic units or lithology can be established

porosities in the reef core are situated. For the third unit, Malm ϵ to Malm α, the entire study area has a negligible to poor reservoir quality, except for some smaller zones in the northeast of the footwall block, and along the Munich Fault with moderate quality.

It has to be noted that this reservoir quality estimation is just based on a porosity evaluation and no permeability values are included. Normally, rock (matrix) permeability is linked to (primary) porosity, for example in sandstones (Albrecht and Reitenbach 2014; Al Saadi et al. 2017; Ganat 2020). However, in our study, area primary porosity is of minor importance and secondary porosity, as described above, is the controlling porosity factor. In addition, regarding permeability, other studies carried out in the GMB, using, e.g., laboratory analysis, hydraulic tests in wells, and numerical modelling, have shown that especially fracture permeability and to a certain part also karst permeability can have a more dominant influence on the hydraulic properties of the reservoir compared to matrix permeability resulting in a mainly fracture- and karst-controlled reservoir (Ehrenberg and Nadeau 2005; Birner et al. 2012; Cacace et al. 2013; Homuth et al. 2015; Moeck et al. 2020; Balcewicz et al. 2021; Bauer et al. 2021). As a result, no general trends describing the porosity–permeability relationship based on stratigraphic units or lithology can be established. This circumstance has already been described for the Molasse Basin, e.g., by Homuth (2014); Bohnsack et al. (2020) and Moeck et al. (2020). Therefore, we cannot directly convert the porosity model into a permeability model and so far, no seismic method exists that is able to derive permeability values from seismic amplitudes or seismic inversion (Pride et al. 2003). However, the improved identification

of karst areas and reefs through the inversion can help to determine zones that might have higher permeability.

Methodical approach

We have shown the applicability of stochastic seismic amplitude inversion and demonstrated its benefits for porosity estimation and characterization of a carbonate reservoir in the GMB. Nevertheless, there are some things to consider regarding the used workflow and the chosen inversion method, from which recommendations for future inversion studies in the GMB can be derived.

The first element that has a big influence on the later inversion result and which partly also influences the choice of the inversion method is the available input data. The 3D seismic data set should always be examined in terms of data quality, especially with regard to the signal-to-noise ratio, the frequency spectrum and the recovery of the true amplitudes. In most cases some preconditioning of the seismic data must be performed to meet these requirements (Veeken and Da Silva 2004). For the GRAME data set most of these objectives have already been taken into account by the contractor during data processing by application of, e.g., filtering, surface-wave noise attenuation and amplitude corrections, such as surface consistent amplitude correction, spherical divergence correction, and predictive deconvolution (Scholze and Wolf 2016a, b). Therefore, the post-stack data set used already had a good data quality for the inversion, except for the frequency spectrum which should be as broadband as possible, but which normally drops off sharply towards the higher frequencies (Zeng 2012). We have partially compensated for this by application of spectral balancing, also called spectral whitening. However, this should only be used with great caution as it can also amplify the high frequency noise, so the results should be checked with spectral analysis and visual inspection before and after whitening like it was done for the GRAME data set. The correct application of frequency spectrum enhancement also leads to an improvement in resolution (Zeng 2012). Other seismic preconditioning methods that might give good results for a different data set could be, e.g., frequency-wavenumber filtering and radon transform or Tau-P processing (Veeken and Da Silva 2004). If an inversion should be carried out, e.g., for other already existing 3D data sets in the GMB, e.g., for Unterhaching or Geretsried, it should be noted that reprocessing may be necessary, to meet the above mentioned requirements.

Another important input data is logging data from wells, in case of availability. Ideally, the number of available wells should correspond to the heterogeneity of the reservoir. Therefore, the more heterogeneous the reservoir, the more boreholes should be implemented into the inversion, to ensure that all possible lithologies and facies types are represented in the well logs (Pendrel 2001). With regard to the carbonate reservoir of the GRAME area, for example, one or two wells might not be sufficient enough to obtain a representative image of the heterogeneously distributed carbonate types as it can be observed in Fig. 5, e.g., Th5 contains mostly dolomitic limestone, Th2a contains mostly dolomite, and Th6 contains mostly limestone. Therefore, implementation of all six available wells and the corresponding well logs delivered a more comprehensive overview of the reservoir. Nonetheless, it should be kept in mind that the wells cover only a limited area of the study site.

Important logs, e.g., for the generation of synthetic seismic traces for the seismic-well tie and the implementation of frequencies outside the seismic bandwidth into the inversion should be measured directly in all wells if possible. At the 'Schäftlarnstraße' geothermal site sonic logs were measured in all six wells for the reservoir section, but in the upper part, sonic logs were only measured in some sections, which is why measurements from several 'Schäftlarnstraße' wells had to be combined to create a continuous log that is required for the seismic-well tie. In the filled up sonic log sections, there will most likely be some uncertainties that will affect the correlation of the reflectors from the seismic data and the reflectors in the synthetic traces. For example, the neighbouring wells might not have drilled the same lithologies in the same depths and the resulting discrepancies can, therefore, influence the quality of the seismic-well tie in these zones. However, this is not the case in the reservoir section, which is our target formation, because direct sonic measurements are available for the reservoir section in all six wells. The direct sonic measurements enable an accurate well-seismic tie for the reservoir formation. The combination of sonic logs and density logs is used to create the synthetic seismic traces on which the seismic-well tie is based and the impedance logs that are used as broadband input parameters for the starting model of the inversion. In our study, like in many others, unfortunately, no density logs were measured, which is why they were determined from the sonic logs based on the Gardner equation, which can lead to uncertainties. For future geothermal drilling projects in the GMB, we recommend that the boreholes are fully surveyed, not only with sonic logs, but also with, e.g., density measurements, if possible.

Reliable high-quality sonic log data is also crucial for the creation of the starting or trend model which enables the calculation of a broad-band impedance model through the inversion process. The stochastic impedance volume derives its lateral resolution from the seismic data, and its vertical resolution from the sonic log data. Therefore, a typical stochastic inversion delivers a vertical resolution of approximately 1 to 2 m (Robinson 2001). In our study the vertical resolution of the impedance model is around 6 m. This limitation is due to the height of the model grid cells that we have specified. In principle, we could have further refined the cell height by implementing even more pseudo-layers. However, this would have resulted in the model consisting of even more grid cells, which would have significantly increased the computing time. The same goes for the number of calculated model realizations. The more realizations are calculated and then combined into an averaged model, the better the model fits to the real geological conditions. In other words, the problem of non-uniqueness is reduced. In our study we calculated 100 realizations of the impedance model and from these 100 models, an averaged model was calculated, which was than used for the interpretation of the acoustic impedance. However, each additional realization also increases the calculation time. To at least reduce this problem, we would, therefore, recommend using larger computing clusters for performing such inversion processes.

There is a also a general trade-off between the quality of the inversion results and the chosen inversion method and the invested time and costs for data acquisition and analysis. In this study, we have shown that full-stack stochastic seismic inversion delivers good results, but newer inversion methods using, e.g., partial stack seismic data offer an even more sophisticated reservoir characterization. Some examples are AVO inversion, simultaneous inversion or time-lapse inversion (Pendrel 2001; Veeken and Da Silva

2004; Filippova et al. 2011; Maleki et al. 2019). In case of amplitude variations with offset (AVO) the inversion should not be performed on fully stacked data. Instead during data processing the traces reflected at a common midpoint should be gathered and sorted by offset, which is related to the incidence angle. For example, the far-offset, the mid-offset, and the near-offset traces can be used to create three different data sets of which each can be inverted separately (Veeken and Da Silva 2004; Barclay et al. 2008). Since seismic amplitude variations with offset contain not only information on the P-impedance, but also on S-impedance and density, AVO inversion delivers more elastic properties describing the reservoir than classical full-stack inversion which delivers only one property. The AVO inversion of the different partial stacks can also be carried out simultaneously, which also enables time-lapse inversion if there are several seismic data sets of the same area measured at different times. This allows to quantify changes in elastic properties due to, e.g., hydrocarbon production (Oldenziel 2003; Barclay et al. 2008; Maleki et al. 2019).

Converting the resulting impedance model into a porosity model strongly relies on a parameter relationship between AI and porosity, which is mostly derived from logging data. Ideally, directly measured porosity logs should be used for this, but if these are not available like in our study, a derived porosity log can be obtained from the sonic logs using Archie's law and the Wyllie time-average equation. However, this procedure can lead to uncertainties in the porosity values. In our study, the derived porosity logs are consistent with results from laboratory analyses of sidewall cores taken from the wells Th4 and Th2 (Pfrang 2020). Thus, verifying the results of the calculated porosity logs. A crossplot of the AI logs and the porosity logs from the six wells was generated and it showed a clear relationship from which a linear function could be derived similar to other studies, e.g., Pendrel and Van Riel (1997); Dohlberg et al. (2000); Zeng (2012). By incorporating the data of all six wells we were able to better represent the heterogeneity of the reservoir in terms of, e.g., lithology and facies distribution, and thus porosity distribution, because even from one well to another the drilled lithologies vary significantly in our study area. If a function would have been used just based on, e.g., Th5 the results would have delivered an AI/porosity relationship that fits for dolomitic limestone, but this function would not have sufficiently taken into account the other carbonate lithology types occurring in the study area, which would have led to inaccuracies. As a consequence, when estimating an AI/porosity relationship in such a heterogeneous reservoir as many data as possible should be incorporated to take all the different lithology and facies types into account to get reliable results. The good representation of the AI/porosity relationship by the linear function is also reflected in the correlation coefficient of 0.75. Based on the linear function, in which low AI correlates with high porosity and high AI with low porosity, the AI volume was converted into a porosity volume to describe the geothermal potential of the reservoir. The calculated porosity model using the linear function was then compared along the drilling paths of the six wells with the corresponding porosity logs to investigate the amount of uncertainty. The comparison shows that the inversion results match the porosity logs by $\pm$ 1% of porosity. Therefore, if we show that the highest porosity in the reefs is 14%, then it could actually also be 13% or 15% because of the uncertainty. This uncertainty is quite small and has, therefore, no significant influence on the classification of the porosity-related reservoir quality, which confirmed our approach.

Taking all this into account, we suggest for future geothermal exploration projects that the possibility of a later inversion should be taken into account when processing the seismic data (preconditioning of the data set). In addition, care should be taken to ensure that well logging data sets are as complete as possible. Then, as a first approach, a stochastic full-stack inversion should be carried out and if this shows promising results, an extended simultaneous AVO inversion can be carried out if necessary. The additionally determined elastic properties, such as the shear impedance and the V_P/V_S ratio could also be used, e.g., in geomechanical modelling and simulations of possible seismicity.

Conclusions and outlook

In this study we demonstrate the benefits of seismic amplitude inversion for porosity estimation and a more detailed structural interpretation of a geothermal carbonate reservoir in the South German Molasse Basin and its implications on reservoir quality. The main findings are:

- Bedded carbonates have parallel to subparallel reflectors with moderate amplitudes and massive carbonates have incoherent and chaotic reflections with low to moderate amplitudes or even transparent areas. Reef buildups have a mound-shaped reflector at the top with semi- to discontinuous reflections directly below and transparent to chaotic reflections in the reef core. Sinkholes and sags are visible as circular indentations truncating the underlying deposits.
- In general, the porosity ranges from zero to around 20% and for the areas along the wells from zero to 14%. The dolomitic limestone has the highest porosities and the calcareous dolomite has the lowest porosities.
- Overall, the footwall of the Munich Fault shows higher porosities than the hanging wall to the south, and the porosity also displays a W–E trend with higher porosities in the western part of the study area.
- Karstification is also more intense north of Munich and along the faults, as indicated by local sinkhole clusters. The sinkholes have porosities of up to 18% on their margins, whereas the center is often characterized by low porosities.
- Carbonate reef buildups and pinnacle reefs were also identified and they show a complex porosity distribution. The reef core has mainly porosities < 3% and the highest porosities of 7 to 14% are observed at the reef cap, in the upper third of the reef and at the reef slopes. This is assumed to be the result of intense karstification and gravitational mass flows on the slopes. At the reef slopes an interfingering of the reef facies with the surrounding strata, in the form of pine tree shaped edges, can be seen. This indicates a syn-sedimentary reef development with slightly varying build up growth rates.
- The reef distribution seems to be oriented parallel to the former passive Tethys margin and, therefore, the Franconian Alb striking in W–E direction and SW–NE direction. The reefs also seem to be larger and better pronounced in the south of Munich compared to the north.
- We defined porosity evaluation levels for reservoir quality assessment. For Berriasian to Malm $\zeta 4$, almost all areas have a moderate to good reservoir quality, especially the northern and northeastern parts of the footwall of the Munich Fault and the south-

western part of the hanging wall. For Malm $\zeta 3$ to Malm $\zeta 1$ the only large areas with moderate quality are found on the footwall and on the hanging wall in the west. For Malm ϵ to Malm α the entire study area has a negligible to poor reservoir quality, except for some smaller zones in the northeast of the footwall block, and along the Munich Fault with moderate quality.

- Preferential targets for geothermal exploitation are the carbonate rocks of Berriasian to Malm $\zeta 1$, in particular, dolomitic limestones due to high porosity and/or strongly karstified areas within bedded and reef facies in the footwall of the Munich Fault and to the west and to the southeast of the hanging wall. The karstification, and therefore, the development of secondary porosity, in these areas, is partly controlled by permeable reef facies at the reef caps and the reef slopes and by faults and their surrounding fracture zones, which enabled more intense fluid migration and thus dissolution and enlargement of the pore space.

To conclude, seismic amplitude inversion and the subsequent porosity estimation are valuable tools to parameterize and characterize the geothermal carbonate reservoir, especially in complex settings, such as heterogeneous carbonates. Therefore, we propose it should be used as a standard seismic method in geothermal exploration.

Based on the results of this study, further investigations to better understand the lithology classification and distribution, and the reef- and karst development should be carried out. These can consist of a seismic multi-attribute analysis that could be used to: (1) understand parameter relationships between seismic attributes and lithology types to create a classification model, (2) analysis of fracture orientations on seismic survey scale and comparisons with investigations at the log scale for a geomechanical characterization, and (3) reconstruction of reef- and karst development.

Abbreviations

AI	Acoustic impedance
GMB	German Molasse Basin
IL	Inline
OMM	Upper Marine Molasse
OSM	Upper Freshwater Molasse
SLS	Schäftlarnstraße
TDR	Time-to-depth relationship
UMM	Lower Marine Molasse
USM	Lower Freshwater Molasse
XL	Crossline

Acknowledgements

We thank the Stadtwerke München (SWM) and the Technical University of Munich for the cooperation and for the seismic and logging data, without which this study could not have been carried out. We also thank two anonymous referees, Johanna Bauer, Hermann Buness and David Tanner for their useful comments that helped to improve the manuscript.

Author contributions

SW carried out the data preparation of the already processed seismic- and logging data as a prerequisite for the inversion (see workflow description in text for details). She also performed the actual inversion workflow, the calculation of the porosity model, the interpretation and discussion of the results, and she wrote the original draft. HvH conceptualized this work, and contributed to the interpretation, the discussion, and writing of the paper. Both authors read and approved the final manuscript.

Funding

Open Access funding enabled and organized by Projekt DEAL. The authors acknowledge financial support by the German Federal Ministry of Economic Affairs and Energy. This study was done in the framework of the project REgine (project number 0324332B), which is part of the joint project GeoMaRe.

Availability of data and materials

The data that support the findings of this study are available from the Stadtwerke München (SWM), the Technical University of Munich (TUM) and the Leibniz Institute of Applied Geophysics (LIAG), but restrictions apply to the availability of these data, which were used under license for the current study, and so are not publicly available. Data are, however, available from the authors upon reasonable request and with permission of SWM, TUM and LIAG.
List of data owners: (1) 3D seismic data ⟶ SWM, (2) Lithology logs of Th1–Th6 ⟶ SWM, (3) Sonic logs of Th1, Th2a, Th3, Th5 and Th6 ⟶ SWM, (4) Sonic log of Th4 ⟶ TUM, (5) Porosity logs of Th1–Th6 ⟶ TUM, (6) Sequence stratigraphic information of the wells Th1–Th6 ⟶ TUM, (7) Structural geological model ⟶ LIAG, (8) Inversion data ⟶ LIAG, and (9) Porosity model ⟶ LIAG.

Declarations

Competing interests

The authors declare that they have no competing interests.

Received: 8 November 2021 Accepted: 22 June 2022
Published online: 11 July 2022

References

Abelson M, Baer G, Shtivelman V, Wachs D, Raz E, Crouvi O, Kurzon I, Yechieli Y. Collapse-sinkholes and radar interferometry reveal neotectonics concealed within the Dead Sea basin. Geophys Res Lett. 2003;30(10):521–3. https://doi.org/10.1029/2003GL017103.

Agemar T, Schellschmidt R, Schulz R. Subsurface temperature distribution in Germany. Geothermics. 2012;44:65–77. https://doi.org/10.1016/j.geothermics.2012.07.002.

Al Saadi F, Wolf K-H, van Kruijsdijk C. Characterization of Fontainebleau Sandstone: Quartz Overgrowth and its Impact on Pore-Throat Framework. J Pet Environ Biotechnol. 2017;8(3):1–12. https://doi.org/10.4172/2157-7463.1000328.

Albrecht D, Reitenbach V. Laboratory measurements of fluid transport properties on tight gas sandstones and applications. Energy Procedia. 2014;59:366–73. https://doi.org/10.1016/j.egypro.2014.10.390.

Andres G. Fränkische Alb und Malmkarst des Molassebeckens - Grundwassergleichenkarte von Bayern 1:500000 mit Erläuterungen. Schriftenreihe Bayerisches Landesamt für Wasserwirtschaft. 1985;20:23–5.

Arthaud F, Matte P. Late Paleozoic strike-slip faulting in southern Europe and northern Africa: result of right lateral shear zone between the Appalachians and the Urals. Bull Geol Soc Am. 1977;88:1305–20.

Bachmann GH, Müller M. Sedimentary and structural evoluion of the German Molasse Basin. Eclogae Geol Helv. 1992;85(3):519–30. https://doi.org/10.5169/seals-167019.

Bachmann GH, Müller M, Weggen K. Evolution of the Molasse Basin (Germany, Switzerland). Tectonophysics. 1987;137(1–4):77–92. https://doi.org/10.1016/0040-1951(87)90315-5.

Balcewicz M, Ahrens B, Lippert K, Saenger EH. Characterization of discontinuities in potential reservoir rocks for geothermal applications in the Rhine-Ruhr metropolitan area (Germany). Solid Earth. 2021;12:35–58. https://doi.org/10.5194/se-12-35-2021.

Barclay F, Bruun A, Rasmussen KB, Alfaro JC, Cooke A, Cooke D, Salter D, Godfrey R, Lowden D, McHugo S, Özdemir H, Pickering S, Pineda FG, Herwanger J, Volterrani S, Murineddu A, Rasmussen A, Roberts R. Seismic inversion: reading between the lines. Oilfield Rev. 2008;20(1):42–63.

Bauer J, Pfrang D, Krumbholz M. Characterisation of a highly heterogeneous geothermal reservoir based on geophysical well logs. EGU General Assem Proc. 2002. https://doi.org/10.5194/egusphere-egu21-2205.

Birner J, Fritzer T, Jodocy M, Savvatis A, Schneider M, Stober I. Hydraulische Eigenschaften des Malmaquifers im Süddeutschen Molassebecken und ihre Bedeutung für die geothermische Erschließung. Z Geol Wiss. 2012;40:133–56.

Böhm F, Savvatis A, Steiner U, Schneider M, Koch R. Lithofazielle Reservoircharakterisierung zur geothermischen Nutzung des Malm im Großraum München. Grundwasser. 2013;18:3–13. https://doi.org/10.1007/s00767-012-0202-4.

Bohnsack D, Potten M, Pfrang D, Wolpert P, Zosseder K. Porosity-permeability relationship derived from Upper Jurassic carbonate rock cores to assess the regional hydraulic matrix properties of the Malm reservoir in the South German Molasse Basin. Geothermal Energy. 2020;8(12):1–47. https://doi.org/10.1186/s40517-020-00166-9.

Bredesen K, Dalgaard E, Mathiesen A, Rasmussen R, Balling N. Seismic characterization of geothermal sedimentary reservoirs: A field example from the Copenhagen area, Denmark. Interpretation. 2020;8(2):T275–91. https://doi.org/10.1190/int-2019-0184.1.

Burgess PM, Winefield P, Minzoni M, Elders C. Methods for identification of isolated carbonate buildups from seismic reflection data. AAPG Bull. 2013;97(7):1071–98. https://doi.org/10.1306/1205121011.

Cacace M, Blöcher G, Watanabe N, Moeck I, Börsing N, Scheck-Wenderoth M, Kolditz O, Huenges E. Modelling of fractured carbonate reservoirs: outline of a novel technique via a case study from the Molasse Basin, southern Bavaria, Germany. Environ Earth Sci. 2013;70(8):3585–602. https://doi.org/10.1007/s12665-013-2402-3.

Closson D, Abou Karaki N. Salt karst and tectonics: sinkholes development along tension cracks between parallel strike-slip faults, Dead Sea. Jordan Earth Surf Process Landforms. 2009;34:1408–21. https://doi.org/10.1002/esp.1829.

Del Prete S, Iovine G, Parise M, Santo A. Origin and distribution of different types of sinkholes in the plain areas of Southern Italy. Geodinamica Acta. 2010;23:113–27. https://doi.org/10.3166/ga.23.113-127.

Dohlberg DM, Helgesen J, Hanssen TH, Magnus I, Saigal G, Pedersen BK. Porosity prediction from seismic inversion, Lavrans Field, Halten Terrace. Norway The Leading Edge. 2000;19(4):392–9. https://doi.org/10.1190/1.1438618.

Dufter C, Reinhold N, Kleinertz B, von Roon S. Wärmewende München 2040-Handlungsempfehlungen: Endbericht. München: Forschungsgesellschaft für Energiewirtschaft mbH (FfE); 2018.

Eaton TT. On the importance of geological heterogeneity for flow simulation. Sediment Geol. 2006;184(3–4):187–201. https://doi.org/10.1016/j.sedgeo.2005.11.002.
Ehrenberg SN. Porosity destruction in carbonate platforms. J Petrol Geol. 2006;29:41–52. https://doi.org/10.1111/j.1747-5457.2006.00041.x.
Ehrenberg SN, Nadeau PH. Sandstone vs. carbonate petroleum reservoirs: a global perspective on porosity-depth and porosity permeability relationships. AAPG Bulletin. 2005;89(4):435–45. https://doi.org/10.1306/11230404071.
Eisbacher GH. Molasse - Alpine and Columbian. Geosci Can. 1974;1:47–50.
Filippova K, Kozhenkov A, Alabushin A. Seismic inversion techniques: choice and benefits. First Break. 2011;29:103–14.
Francis AM. Understanding stochastic inversion: part 1. First Break. 2006;24(11):69–77. https://doi.org/10.3997/1365-2397.2006026.
Francis AM. Understanding stochastic inversion: part 2. First Break. 2006;24(12):79–84. https://doi.org/10.3997/1365-2397.2006028.
Freudenberger W, Schwerd K. Erläuterungen zur Geologischen Karte von Bayern 1:500000. München: Bayer. Geolog. Landesamt; 1996.
Frisch W. Tectonic progradation and plate tectonic evolution of the Alps. Tectonophysics. 1979;60(3–4):121–39. https://doi.org/10.1016/0040-1951(79)90155-0.
Ganat TA-AO. Fundamentals of Reservoir Rock Properties. Berlin: Springer; 2020.
Ghafoori MR, Roostaeian M, Sajjadian VA. Secondary porsity: A Key Parameter Controlling the Hydrocarbon Production in Hetereogeneous Carbonate Reservoirs (Case Study). Petrophysics. 2009;50:67–78.
Gogoi T, Chatterjee R. Estimation of petrophysical parameters using seismic inversion and neural network modeling in Upper Assam basin, India. Geosci Front. 2019;10:1113–24. https://doi.org/10.1016/j.gsf.2018.07.002.
Gutiérrez F, Guerrero J, Lucha P. A genetic classification of sinkholes illustrated from evaporite paleokarst exposures in Spain. Environ Geol. 2008;53(5):993–1006. https://doi.org/10.1007/s00254-007-0727-5.
Haas A, Dubrule O. Geostatistical inversion-a sequential method of stochastic reservoir modelling constrained by seismic data. First Break. 1994;12(11):561–9. https://doi.org/10.3997/1365-2397.1994034.
Hill SJ. Inversion-based thickness determination. Leading Edge. 2005;25(5):477–80. https://doi.org/10.1190/1.1926799.
Homuth S, Göth AE, Sass I. Reservoir characterization of the Upper Jurassic geothermal target formations (Molasse Basin, Germany): role of thermofacies as exploration tool. Geotherm Energy Sci. 2015;3:41–9. https://doi.org/10.5194/gtes-3-41-2015.
Hopley D. Encyclopedia of Modern Coral Reefs: Structure, Form and Process. New York: Springer; 2011.
Jarvis K, Folkers A, Mesdag P. Reservoir characterization of the Flag Sandstone, Barrow Sub-basin, using an integrated, multiparameter seismic AVO inversion technique. Leading Edge. 2004;23(8):798–800. https://doi.org/10.1190/1.1786906.
Jodocy M, Stober I. Geologisch-geothermische Tiefenprofile für den südwestlichen Teil des Süddeutschen Molassebeckens. Zeitschrift der Deutschen Gesellschaft für Geowissenschaften. 2009;160(4):359–66. https://doi.org/10.1127/1860-1804/2009/0160-0359.
Kendall C, Schlager W. Caronates and relative changes in sea level. Marine Geol. 1981;44(1–2):181–212. https://doi.org/10.1016/0025-3227(81)90118-3.
Kenkmann T, Hesse T, Hülsmann F, Timpe C, Hoppe K. Klimaschutzziel und -strategie München 2050 - Endbericht. Freiburg: Institut für angewandte Ökologie; 2017.
Koch R. Die neue Interpretation der Massenkalke des Süddeutschen Malm und ihr Einfluß auf die Qualität von Kalksteinen für technische Anwendungen. Archaeopterix. 2000;18:43–65.
Koltermann CE, Gorelick SM. Heterogeneity in sedimentary deposits: a review of structure-imitating, process-imitating, and descriptive approaches. Water Resour Res. 1996;32(9):2617–58. https://doi.org/10.1029/96WR00025.
Konrad F, Savvatis A, Wellmann F, Zosseder K. Hydraulic behavior of fault zones in pump tests of geothermal wells: a parametric analysis using numerical simulations for the Upper Jurassic aquifer of the North Alpine Foreland Basin. Geothermal Energy. 2019;7(1):1–28. https://doi.org/10.1186/s40517-019-0137-4.
Lemcke K. Zur nachpermischen Geschichte des nördlichen Alpenvorlandes. Geol Bavarica. 1973;69:5–48.
Lemcke K. Das bayerische Alpenvorland vor der Eiszeit: Erdgeschichte-Bau-Bodenschätze. Stuttgart: Schweizerbart; 1988.
Lindseth RO. Synthetic sonic logs—a process for stratigraphic interpretation. Geophysics. 1979;11(1):3–26.
Lucia FJ. Carbonate reservoir characterization: an integrated approach. Berlin: Springer; 2007.
Lüschen E, Dussel M, Thomas R, Schulz R. 3D seismic survey for geothermal exploration at Unterhaching, Munich, Germany. First Break. 2011;29(1):45–54. https://doi.org/10.3997/1365-2397.2011002.
Lüschen E, Wolfgramm M, Fritzer T, Dussel M, Thomas R, Schulz R. 3D seismic survey explores geothermal targets for reservoir characterization at Unterhaching, Munich, Germany. Geothermics. 2014;50:167–79. https://doi.org/10.1016/j.geothermics.2013.09.007.
Mahgoub MI, Padmanabhan E, Abdulatif OM. Seismic inversion as a predictive tool for porosity and facies delineation in Paleocene fluvial/lacustrine reservoirs, Melut Basin, Sudan. Marine Petrol Geol. 2017;86:213–27. https://doi.org/10.1016/j.marpetgeo.2017.05.029.
Mahgoub MI, Padmanabhan E, Abdulatif OM. Facies and porosity 3D models constrained by stochastic seismic inversion to delineate Paleocene fluvial/lacustrine reservoirs in Melut Rift Basin, Sudan. Marine Petrol Geol. 2018;98:79–96. https://doi.org/10.1016/j.marpetgeo.2018.08.003.
Marfurt KJ. Techniques and best practices in multiattribute display. Interpretation. 2015;3(1):B1–23. https://doi.org/10.1190/INT-2014-0133.1.
Mavko G, Mukerji T, Dvorkin J. The Rock Physics Handbook Tools for Seismic Analysis of Porous Media. Cambridge: Cambridge University Press; 2009.
Mehrabi H, Ranjbar-Karami R, Roshani-Nejad M. Reservoir rock typing and zonation in sequence stratigraphic framework of the Cretaceous Dariyan Formation, Persian Gulf. Carbonates Evap. 2019;34:1833–53. https://doi.org/10.1007/s13146-019-00530-2.
Moeck I, Dussel M, Weber J, Schintgen T, Wolfgramm M. Geothermal play typing in Germany, case study Molasse Basin: a modern concept to categorise geothermal resources related to crustal permeability. Netherlands J Geosc. 2020;98(e14):1–10. https://doi.org/10.1017/njg.2019.12.

Nascimento TM, Menezes PTL, Braga IL. High-resolution acoustic impedance inversion to characterize turbidites at Marlim Field, Campos Basin, Brazil. Interpretation. 2014;2(3):T143–53. https://doi.org/10.1190/INT-2013-0137.1.
Pendrel J. Seismic inversion–the best tool for reservoir characterization. CSEG Recorder. 2001;26(1):1–12.
Pendrel J, Van Riel P. Methodology for Seismic Inversion, A Western Canadian Reef Example. CSEG Recorder. 1997;22(5):1–16.
Pieńkowski G, Schudack ME, Bosák P, Enay R, Feldman-Olszewska A, Golonka J, Gutowski J, Herngreen GFW, Jordan P, Krobicki M, Lathuiliere B, Leinfelder RR, Michalik J, Mönnig E, Noe-Nygaard N, Pálfy J, Pint A, Rasser MW, Reisdorf AG, Schmid DU, Schweigert G, Surlyk F, Wetzel A, Wong TE. Jurassic. In: McCann T, editor. The Geology of Central Europe Volume 2: Mesozoic and Cenozoic. The Geological Society: London; 2008. p. 823–922.
Pride SR, Harris JM, Johnson DL, Mateeva A, Nihei KT, Nowack RL, Rector JW, Spetzler H, Wu R, Yamomoto T, Berryman JG, Fehler M. Permeability dependence of seismic amplitudes. Leading Edge. 2003;22(6):518–25. https://doi.org/10.1190/1.1587671.
Pussak M, Bauer K, Stiller M, Bujakowski W. Improved 3D seismic attribute mapping by CRS stacking instead of NMO stacking: Application to a geothermal reservoir in the Polish Basin. J Appl Geophys. 2014;103:186–98. https://doi.org/10.1016/j.jappgeo.2014.01.020.
Quenstedt FA. Der Jura. Tübingen: H. Laupp Publishing; 1858. p. 842.
Rashad O, El-Barkooky AN, El-Araby A, El-Tonbary M. Deterministic and Stochastic Seismic Inversion techniques towards a better prediction for the reservoir distribution in NEAG-2 Field, north Western Desert, Egypt. Egypt J Petrol. 2022;31(1):15–23. https://doi.org/10.1016/j.ejpe.2021.12.002.
Reinhold C. Multiple episodes of dolomitization and dolomiterecrystallization during shallow burial in Upper Jurassic shelf carbonates: eastern Swabian Alb, southern Germany. Sediment Geol. 1998;121:71–95.
Robinson G. Stochastic seismic inversion applied to reservoir characterization. CSEG Recorder. 2001;26(1):1–12.
Sajed OKM, Glover PWJ. Dolomitisation, cementation and reservoir quality in three Jurassic and Cretaceous carbonate reservoirs in north-western Iraq). Marine Petrol Geol. 2020;115:1–20. https://doi.org/10.1016/j.marpetgeo.2020.104256.
Sams M, Carter D. Stuck between a rock and a reflection: A tutorial on low-frequency models for seismic inversion. Interpretation. 2017;5(2):B17–27. https://doi.org/10.1190/INT-2016-0150.1.
Schmoker JW, Halley RB. Carbonate porosity versus depth: a predictable relation for south Florida. Am Assoc Petrol Geol Bull. 1982;66(12):2561–70.
Schölderle F, Lipus M, Pfrang D, Reinsch T, Haberer S, Einsiedl F, Zosseder K. Monitoring cold water injections for reservoir characterization using a permanent fiber optic installation in a geothermal production well in the Southern German Molasse Basin. Geotherm Energy. 2021;9(21):1–36. https://doi.org/10.1186/s40517-021-00204-0.
Shankar U, Ojha M, Ghosh R. Assessment of gas hydrate reservoir from inverted seismic impedance and porosity in the northern Hikurangi margin. Marine Petrol Geol. 2021;123:1–13. https://doi.org/10.1016/j.marpetgeo.2020.104751.
Shipilin V, Tanner DC, von Hartman H, Moeck I. Multiphase, decoupled faulting in the southern German Molasse Basin - evidence from 3-D seismic data. Solid Earth. 2020;11:2097–117. https://doi.org/10.5194/se-11-2097-2020.
Słonka Ł, Krzywiec P. Seismic Characteristics and Development of the Upper Jurassic Carbonate Buildups from the Miechów Trough (Southern Poland). Geosciences. 2020;10(239):1–32. https://doi.org/10.3390/geosciences10060239.
Stober I. Hydrochemical properties of deep carbonate aquifers in the SW German Molasse Basin. Geothermal Energy. 2014;2(1):13. https://doi.org/10.1186/s40517-014-0013-1.
Stober I, Villinger E. Hydraulisches Potential und Durchlässigkeit des höheren Oberjuras und des Oberen Muschelkalks unter dem badenwürttembergischen Molassebecken. Jahreshefte Geologisches Landesamt Baden-Württemberg. 1997;37:77–96.
Stober I, Jodocy M, Burisch M, Person R. Tiefenwässer im Oberen Muschelkalk-Aquifer des Oberrheingrabens und des Südwestdeutschen Molassebeckens. Grundwasser. 2013;18(2):117–27. https://doi.org/10.1007/s00767-013-0224-6.
Veeken PCH, Da Silva M. Seismic inversion methods and some of their constraints. First Break. 2004;22:15–38. https://doi.org/10.3997/1365-2397.2004011.
Wadas SH, Tanner DC, Polom U, Krawczyk CM. Structural analysis of S-wave seismics around an urban sinkhole; evidence of enhanced dissolution in a strike-slip fault zone. Nat Hazard Earth Sys. 2017;17:2335–50. https://doi.org/10.5194/nhess-17-2335-2017.
Wang Y, Eichkitz CG, Schreilechner MG, Heinemann G, Davis JC, Gharsalla M. Seismic attributes for description of reef growth and channel system evolution - Case study of Intisar E Libya. Interpretation. 2015;4:1–11. https://doi.org/10.1190/INT-2015-0017.1.
Xu X, Chen Q, Chu C, Li G, Liu C, Shi Z. Tectonic evolution and paleokarstification of carbonate rocks in the Paleozoic Tarim Basin. Carbonates Evapor. 2017;32(4):487–96. https://doi.org/10.1007/s13146-016-0307-4.
Yilmaz Ö. Seismic Data Analysis: Processing, Inversion, and Interpretation of Seismic Data. Tulsa: Soc. Explor. Geophys; 2001.
Zhang R, Sen MK, Phan S, Srinivasan S. Stochastic and deterministic seismic inversion methods for thin-bed resolution. J Geophys Eng. 2012;9:611–8. https://doi.org/10.1088/1742-2132/9/5/611.
Ziegler PA. Late Cretaceous and Cenozoic intraplate compressional deformations in the Alpine foreland - a geodynamic model. Tectonophysics. 1987;137:399–420. https://doi.org/10.1016/0040-1951(87)90330-1.
Böhm F. PhD thesis: Die Lithofazies des Oberjura (Malm) im Großraum München und deren Einfluss auf die tiefengeothermische Nutzung. Freie Universität Berlin, 2012.
Böhm F, Dax M. Lithology logs of boreholes Th1, Th2a, Th3, Th4, Th5, and Th6 of the geothermal site Schäftlarnstraße in Munich based on mudlogging data carried out on behalf of the Munich City Utilities (SWM). Personal communication, 2019.
Doyen PM. Seismic Reservoir Characterization - An Earth Modelling Perspective. EAGE Publications, 2007.
Hänel R, Kleefeldt M, Koppe I. Geothermisches Energiepotenzial. Pilotstudie: Abschätzung der geothermischen Energievorräte an ausgewählten Beispielen in der Bundesrepublik Deutschland (Abschlussbericht). Bericht NLfB (im Auftrag der Europäischen Gemeinschaft und des Bundesminitseriums für Forschung und Technologie. 1984. Archive number: 96 276, Volume I–IV, Hannover.
Hill SJ, Rüger A. Illustrated Seismic Processing Volume 1: Imaging. Soc. Explor. Geophys., Tulsa, USA, 2019.
Homuth S. PhD thesis: Aufschlussanalogstudie zur Charakterisierung oberjurassischer geothermischer Karbonatreservoire im Molassebecken. Technical University Darmstadt, Germany, 2014.

Lucia FJ, Kerans C, Senger RK. Defining flow units in dolomitized carbonate-ramp reservoirs: SPE annual technical conference and exhibition, 4-7 October, Washington, D.C.: Society of Petroleum Engineers; 1992. https://doi.org/10.2118/24702.
Maleki M, Davolio A, Schiozer DJ. Closing the Loop Between 4D Seismic Inverted Impedance and Engineering Data: Norne Field. In: 81st EAGE Conference and Exhibition - Conference Proceedings. 2019; 1–5. https://doi.org/10.3997/2214-4609.201900929.
Moore CH. Developments in Sedimentology Vol. 55 – Carbonate Reservoirs: Porosity, Evolution and Diagenesis in a Sequence Stratigraphic Framework. Amsterdam: Elsevier; 2001.
Mountjoy EW, Marquez XM. Predicting Reservoir Properties in Dolomites: Upper Devonian Leduc Buildups, Deep Alberta Basin. In: Kupecz JA, Gluyas J & Bloch S. (eds): Reservoir quality prediction in sandstones and carbonates. AAPG Memoir. 1997; 69:267–306.
Mraz E. PhD thesis: Reservoir characterization to improve exploration concepts of the Upper Jurassic in the Southern Bavarian Molasse Basin. Technische Universität München, 2019. url: http://nbn-resol ving.de/urn/resolver.pl?urn:nbn:de:bvb:91-diss-20190 430-14640 81-1-6.
Oldenziel T. PhD thesis: Time-lapse seismic within reservoir engineering. Technical University Delft, 2003.
Pavlova MA, Reid I. Geophysical Inversion of 3D Seismic Data in Panax's Limestone Coast Geothermal Project to Determine Reservoir Porosity. Proceedings World Geothermal Congress - Bali, Indonesia, 25-29 April 2010. url: https://www.geothermal-energy.org/pdf/IGAstandard/WGC/2010/1318.pdf
Pfrang D. Estimated porosity logs of the six wells of the geothermal site Schäftlarnstraße. Personal communication, 2020.
Schmid DU, Leinfelder RR, Schweigert G. Stratigraphy and palaeoenvironments of the Upper Jurassic of Southern Germany - a review. Proceedings of the 4th Int. Symposium on Lithographic Limestone and Plattenkalk. 2005; 31–41.
Scholze M, Wolf F. GRAME 3D- und 2D-Seismik München Süd - Bericht zur seismischen Datenbearbeitung im Zeitbereich; unpublished report. DMT Petrologic GmbH; 2016a.
Scholze M, Wolf F. GRAME 3D- und 2D-Seismik München Süd - Bericht zur seismischen Datenbearbeitung im Tiefenbereich; unpublished report. DMT Petrologic GmbH; 2016b.
Sell A, Buness H, Tanner D, Ziesch J, Weller A. FD modelling of deeply-buried paleo-dolines underneath the city of Munich. EAGE Near Surface Geoscience Conference and Exhibition, 1st Conference on Geophysics for Geothermal and Renewable Energy Storage. 2019.
Steiner U, Savvatis A, Böhm F, Schubert A. Explorationsstrategie tiefer geothermischer Ressourcen am Beispiel des süddeutschen Oberjuras (Malm). 2014:429–61. https://doi.org/10.1007/978-3-642-54511-5_13.
SWM - Stadtwerke München (Munich City Utilities). Sonic log data of boreholes Th1, Th2a, Th3, Th5, and Th6 of the geothermal site Schäftlarnstraße in Munich. Personal communication, 2019.
Tiab D, Donaldson EC. Petrophysics: Theory and Practice of Measuring Reservoir Rock and Fluid Transport Properties. Gulf Professional Publishing, 2015.
Wadas SH, Tschache S, Polom U, Krawczyk CM. Sinkhole imaging and identification of fractures with S_H-wave reflection seismic. 15th Multidisciplinary Conference on Sinkholes and the Engineering and Environmental Impacts of Karst 2018, Shepherdstown, West Virginia, USA.
Wolfgramm M, Dussel M, Koch R, Lüschen E, Schulz R, Thomas R. Identifikation und Charakterisierung der Zuflusszonen im Malm des Molassebeckens nach petrographisch-faziellen und geophysikalischen Daten. Proceedings – Der Geothermiekongress, Bochum, Germany, 2011.
Wolpert P, Pfrang D, Bohnsack D, Beichel K, Bauer J. Sequence stratigraphic Workshop on the six wells of the geothermal site Schäftlarnstraße. Technical University Munich, 30.09.2020; personal communication, 2020.
Zeng H. Construction and Analysis of Three-Dimensional Seismic Porosity Inversion Models. In: Ruppe SC, editor. Anatomy of a giant carbonate reservoir: Fullerton Clear Fork (Lower Permian) field, Permian Basin, Texas. Studies in Geology. 2012; 63:93–110. doi: 0.1306/13341540St633003.
Ziegler PA. Geological Atlas of Western and Central Europe. B.V., The Hague: Shell Internationale Petroleum Maatschappij; 1990.
Ziesch J. Kapitel 4.3: 3D-Strukturanalyse und Retrodeformation. In: Endbericht GeoParaMol - Bestimmung von relevanten Parametern zur faziellen Interpretation des Malm und Modellierung des thermisch-hydraulischen Langzeitverhaltens. Project report for the German Ministry of Economic Affairs. 2019; 51–63. https://doi.org/10.2314/KXP:1678714100.

Publisher's Note